

FRIEDRICH SCHILLER UNIVERSITY OF JENA

FACULTY OF PHYSICS AND ASTRONOMY

Master's Thesis in Photonics

**Retrospective reconstruction of knee CINE images
from continuous radial magnetic resonance imaging
using a knee loading device**

By

Martin ALEKSIEV



**FRIEDRICH-SCHILLER-
UNIVERSITÄT
JENA**

FRIEDRICH SCHILLER UNIVERSITY OF JENA

FACULTY OF PHYSICS AND ASTRONOMY

A thesis submitted in partial fulfillment of the requirements for the degree
of M.Sc. Photonics

**Retrospective reconstruction of knee CINE images
from continuous radial magnetic resonance imaging
using a knee loading device**

Author: B. Sc. Martin ALEKSIEV

Supervisor: Prof. Dr. rer. nat. med. habil. Jürgen R. REICHENBACH

Supervisor: Dr. rer. nat. Martin KRÄMER

Submission date: November 01, 2021

CONTENTS

I	Introduction	4
II	Theory	5
II-A	Fundamentals	5
II-B	RF excitation	6
II-C	Free Induction Decay (FID)	6
II-D	Spatial encoding	7
II-E	K-space representation	8
II-F	Fourier Transform	9
II-G	Radial MRI using an azimuthal increment based on the Golden Ratio	9
II-H	Gradient Echo sequence	10
II-I	Multi-slice sequence	11
II-J	3D UTE sequence	12
III	Methods and Materials	13
III-A	Description of the Device	13
III-B	Data synchronisation and reconstruction	16
III-C	Measurements	19
IV	Results	26
IV-A	Real-time and CINE images from the 30 bpm measurement with weight	26
IV-B	CINE images for 3 measurements with different motion speed	30
IV-C	High resolution CINE images	30
IV-D	Transverse and sagittal shifts of the leg	31
IV-E	Golden angle and continuous golden angle CINE images	34
IV-F	Multi-slice and 3D UTE images	36
IV-G	Comparing CINE images of measurements with and without weight	40
V	Discussion	40
VI	Conclusion	44
References		45

I. INTRODUCTION

Magnetic Resonance Imaging (MRI) is a powerful imaging modality that can be used to evaluate musculoskeletal joint conditions with superb soft-tissue contrast and non-ionising electro-magnetic fields [1]. "Magnetic" refers to the use of an assortment of magnetic fields and "resonance" refers to the need to match the frequency of an oscillating magnetic field with the precessional frequency of the spin of a nucleus in a tissue molecule [2]. The non-ionising nature of the electro-magnetic fields makes the repeated application of MRI relatively safe with no known relevant side effects [3].

Magnetic Resonance Imaging acquires complex-valued data points in a spatial frequency domain called k-space [1], which contains the spatial frequency information of the measured signals. This data can then be Fourier transformed to obtain an image of the recorded information [4] (a process also called image reconstruction). Different techniques of filling k-space have been developed such as Cartesian [5], radial [6] and many others, each of which has different advantages and disadvantages depending on the intended application. For example, data points acquired with Cartesian sequences are regularly spaced in comparison to data points acquired using radial sequences, which need to be additionally interpolated onto a Cartesian grid (a process called gridding) before Fourier transform computations. This makes Cartesian techniques preferable to radial ones when the subject is stationary [7]. Radial sequences, however, may be preferred for dynamic imaging (i.e., when the subject is moving a joint inside the scanner during data acquisition), because the resulting images are less sensitive to motion artifacts compared to Cartesian sequences [8]. Additionally, using the golden angle as an azimuthal increment to acquire data in radial k-space offers higher

flexibility for retrospective selection of data for reconstruction [8].

The knee is one of the most commonly injured joints from sport activities, and trauma to it can cause functional limitations, leading to a substantially lower quality of life in patients [9]. Stationary and unloaded conditions do not portray the dynamic physiology of joints and may prevent the detection of functional deficiencies. Evaluation of musculoskeletal joint conditions is particularly relevant in the context of motion as abnormal motion of the knee can be linked to degenerative changes of the knee. For example, abnormal mechanics due to anterior cruciate ligament injury are implicated in the development of knee osteoarthritis [10]. There is therefore value in investigating methods for acquiring and reconstructing images from dynamic MRI data with higher spatial resolution.

In the context of MR imaging of knee motion, several challenges arise. In general, hundreds of readouts may be necessary to reconstruct a single image with a fully sampled k-space, and acquisition of these readouts may be overall slower than the knee motion. To cope with this, sequences have been developed for faster imaging such as Fast Low Angle Shot (FLASH) [11] MRI, for which the sequence repetition time (TR) and the flip angle are reduced. Additionally, different reconstruction techniques such as CINE have been developed, which allow image reconstruction from repetitive motion. CINE is a technique often used in cardiac imaging where images are reconstructed from readouts acquired during the same phase in multiple cardiac cycles [12], due to the short duration of the cycle. By displaying several static images from subsequent phases in the cardiac cycle in succession, it is possible to create a movie of the beating heart (analogous to using individual images from a camera to create a movie) which

could offer more insight to cardiac research and medical examination than a static image. In the context of this work, CINE is used to reconstruct images with readouts acquired during the same phase of knee motion in cycles of flexion and extension. Another challenge is the knee motion itself, as repetitive motion cycles require a device or setup that guides the leg through the flexion-extension motion to reduce undesired displacement that may occur. Such unwanted displacement would be a problem for CINE images, because readouts acquired during different motion cycles could capture the leg at different positions in space, resulting in blurred CINE images. Additionally, it is essential that such a device is made from non-magnetic materials, fits inside the bore of an MR scanner and allows a suitable range of motion of the knee, for example 30° of knee flexion. Typically, some kind of synchronisation trigger is required to know which readouts were acquired during the same phase in the motion cycle. Examples of such synchronisation triggers used for joint motion are optical triggers marking the end of knee extension [13] and pseudo-ECG (electrocardiogram), achieved using a pressure transducer attached to a region of skin-muscle shifting, a respiratory monitor and an active differentiator [14].

In this work, a rotary encoder (angular position sensor) is used together with an MRI safe knee loading device to record the angular position of the knee motion during MR measurements. By synchronising the data from the rotary encoder with the acquired MRI data, it becomes possible to reconstruct knee images at a specific angular position and range of angles (referred to as angle window), which allows for CINE reconstruction.

The goal was to reconstruct CINE images from repetitive knee motion and compare them to real-

time reconstructed images (i.e., using readouts acquired during a single flexion-extension motion cycle), as well as demonstrate the capabilities of CINE reconstruction that could improve future investigations of knee injuries. To compare CINE and real-time (RT) images, two-dimensional (2D) slices of the knee were acquired using radial MRI sequences with the golden angle [8] as an azimuthal increment. The capabilities of CINE were demonstrated by reconstructing images for different reconstruction parameters (angular positions and angle windows), data with different motion speeds and high resolution data. Additionally, CINE images were reconstructed from multi-slice (i.e., capturing more than 1 slice) and 3D UTE (Ultra short Echo Time) data, to capture a larger spatial coverage of the knee. 3D UTE is a sequence that not only captures the whole knee, but also detects tissues with fast signal decay such as tendons, which is valuable to practical applications such as morphological analysis. Due to potential limitations of the device setup, leg displacement and reproducibility were investigated

II. THEORY

A. Fundamentals

In Magnetic Resonance Imaging, the hydrogen protons in the human body interact with an external static magnetic field B_0 . As the proton is a charged particle and is spinning about its axis, it produces its own magnetic field as shown in Figure 1. The proton acts as a magnetic dipole, with its north/south axis represented by the magnetic moment μ [15]. In the absence of B_0 , the magnetic moments of the hydrogen protons in the tissue or sample are oriented randomly and hence do not result in a net magnetisation. In the presence of B_0 , the magnetic moments tend to align themselves towards the external magnetic field and the protons

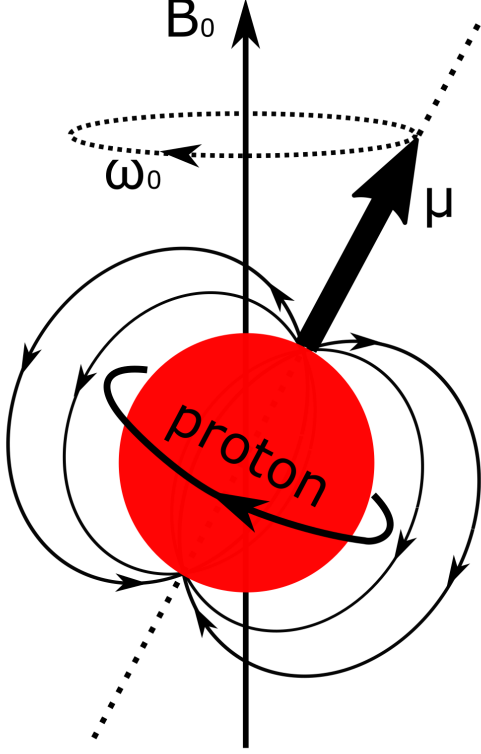


Fig. 1: Diagram of a spinning proton in the presence of an external field B_0 , with magnetic moment μ and precession frequency ω_0 .

precess around the field direction with angular frequency:

$$\omega_0 = -\gamma B_0 \quad (1)$$

where γ is the nuclei-dependent gyromagnetic ratio with SI unit radian per second per tesla ($\text{rad} \cdot \text{s}^{-1} \cdot \text{T}^{-1}$) and ω_0 is called the Larmor frequency [2]. The interaction between the magnetic moments and B_0 results in a net magnetisation M which points in the direction of B_0 .

B. RF excitation

To measure the magnetisation of the system, the direction of the net magnetisation M must be tipped away from B_0 [2]. To perturb the system, a radio frequency (RF) magnetic field B_1 , oscillating at the Larmor frequency, is applied perpendicular

to B_0 for a short time using a transmitter coil. The net magnetisation direction is rotated away from the B_0 longitudinal direction [2] and after the RF pulse duration τ , the direction of M will be at an angle α (called flip angle) away from B_0 , given by:

$$\alpha = \gamma B_1 \tau. \quad (2)$$

In a fixed laboratory frame, the direction of M is rotated away from B_0 in a spiral motion. For a simpler visualisation, this motion is often illustrated in a reference frame rotating about B_0 at the Larmor frequency [2] as shown in Figure 2.

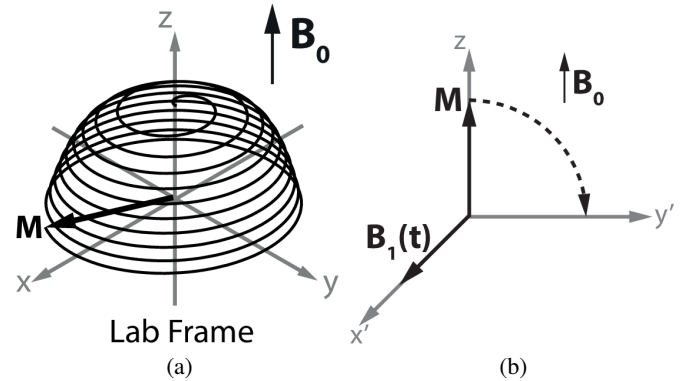


Fig. 2: The direction of M being rotated away from B_0 in a laboratory (a) and rotating (b) reference frame [16].

C. Free Induction Decay (FID)

The precessing transverse magnetisation M_{xy} induces an electromotive force (emf) in a receive coil according to Faraday's law [17]. After the RF pulse duration τ , a relaxation process takes place during which the direction of M tends to return to the direction of B_0 . The recovery of M_z is characterised by the "spin-lattice" relaxation time constant T_1 [18] and results from interactions between the proton spins and their surroundings [2]. It follows an exponential trend shown in Figure 3 and is described by the following equation:

$$M_z(t) = M_0(1 - e^{\frac{-t}{T_1}}). \quad (3)$$

The "spin-spin" decay of M_{xy} results from dephas-

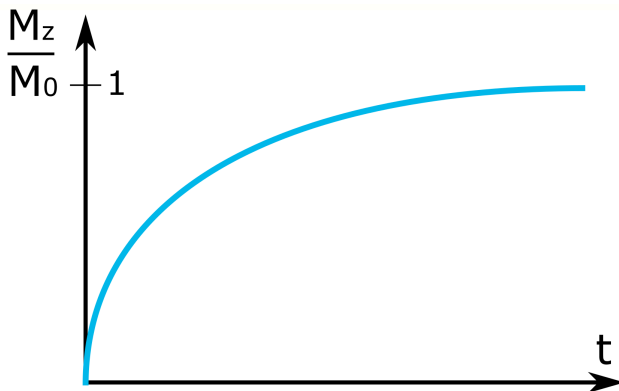


Fig. 3: Recovery of the longitudinal magnetisation M_z following a 90° RF pulse. The recovery produces an exponential curve characterised by the T_1 time constant shown in equation (3) [19].

ing of the protons and is characterised by the T_2 time constant according to the following equation:

$$M_{xy}(t) = M_0 \cdot e^{\frac{-t}{T_2}}. \quad (4)$$

Inhomogeneities in B_0 result in additional dephas-

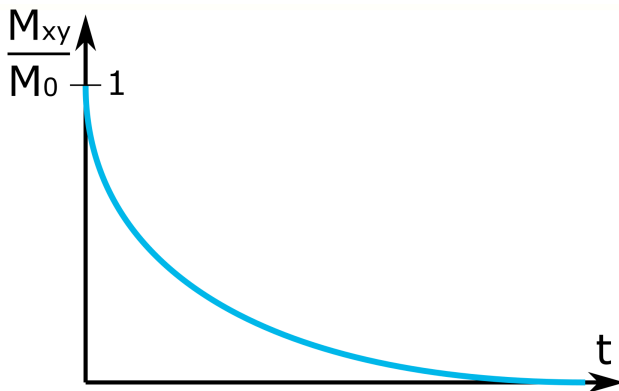


Fig. 4: Transverse magnetisation M_{xy} decay following a 90° RF pulse. The decay produces an exponential curve characterised by the T_2 time constant shown in equation (4).

ing and further reduction of M_{xy} . To take this effect into account, the time constant T_2^* is used:

$$\frac{1}{T_2^*} = \frac{1}{T_2} + \gamma \Delta B_0 \quad (5)$$

where ΔB_0 are the B_0 field inhomogeneities. Additional dephasing from "spin-spin" decay results in a decaying emf signal called free induction decay (FID).

D. Spatial encoding

Spatial encoding is necessary for localising each signal in 3D space and is achieved by applying linear one-dimensional magnetic field gradients in the x-, y- and z-direction. These gradients are generated by wire coils that are located in the bore of the magnet. A gradient along the z-direction G_z is used simultaneously as the applied RF pulse to excite a 2D slice of the human body. The magnetic field experienced by the protons along the z-direction can now be described by:

$$B_z(z) = B_0 + G_z \cdot z. \quad (6)$$

The RF pulse typically has a sinc waveform shape in the time domain. In the frequency domain, it has an approximately rectangular waveform shape, limited by its finite duration [1], and is used when a uniform slice profile is desired. Both the RF pulse bandwidth $\Delta\omega$ and the amplitude of the slice selection gradient G_z can be altered to influence which protons are excited, namely only the protons with precession frequencies inside the pulse bandwidth as shown in Figure 5.

Once a slice is excited, two additional gradients are used to spatially encode the signal along the x- and y-directions. A phase-encoding gradient G_y is applied for a limited time to dephase the precession of the protons and thus spatially encode the signal along the y-direction as shown in Figure 6. With the gradient being switched on, the precession frequencies are changed in a linear fashion. Thus, a signal from a different position along the y-axis will have a different frequency associated with it. After switching off the gradient, the precession

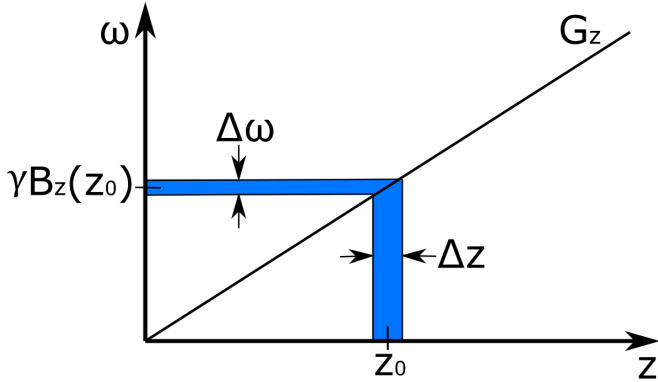


Fig. 5: Slice selection centred at position z_0 along the z axis with thickness Δz , for an RF pulse with bandwidth $\Delta\omega$ and gradient G_z . Only the protons inside the blue-shaded region along the z axis will be excited.

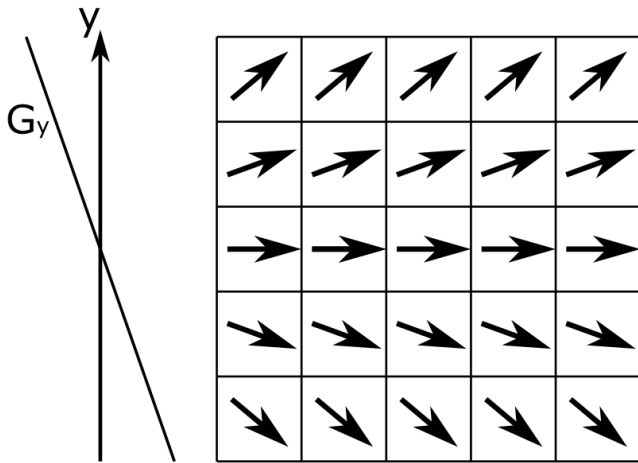


Fig. 6: Phase encoding along the y -direction for a slice with 25 voxels, with the arrows in each voxel representing the precessing protons.

along the y -direction resumes with the same frequency, but now with a linear change in phase as shown by the different rotations of the arrows in Figure 6. A frequency-encoding gradient G_x , applied along the x -direction, is used to linearly alter the precession frequencies along the x -axis similarly to G_y . The frequency encoding gradient is often called the readout-gradient, as data points are acquired during its application.

E. K-space representation

Applying these gradients and recording a signal via the receiver coil stores information about the frequency of a signal and where it originates from in a spatial frequency domain called k-space [20]. The k-space domain is Fourier conjugate to the spatial/image domain and the coordinates k_x and k_y can be expressed by:

$$k_{x/y}(t) = \frac{\gamma}{2\pi} \int_0^t G_{x/y}(\tau) d\tau. \quad (7)$$

The coordinates k_x and k_y do not correspond directly to the spatial domain coordinates x and y of an image. Typically, k-space data is acquired in a Cartesian coordinate system with a centre, which represents low spatial frequency information. An example of what k-space of an image looks like can be seen in Figure 7. Points closer

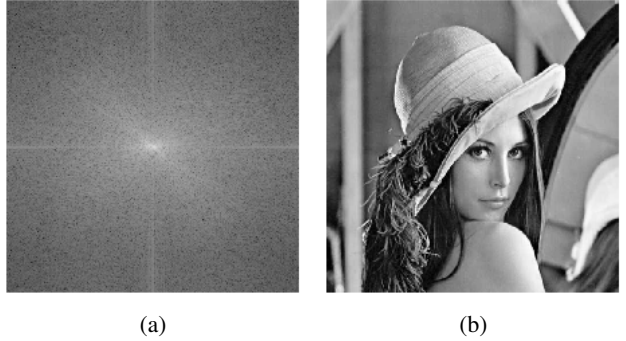


Fig. 7: K-space representation (a) of a well-known standard test image "Lenna" used for image processing (b). The logarithm of the k-space signal is displayed in (a) to better display the high spatial frequency information.

to the k-space centre are responsible for the overall image shape and points further away from it represent higher spatial frequency information, which is responsible for edges and finer details. In the simplest scenario, k-space lines are parallel, equidistant and are recorded one by one, with one line in k-space representing one use of the

RF pulse, the slice selection, phase encoding and frequency encoding gradients. Repeating the sequence of RF pulses and gradients with a different phase encoding gradient G_y stores information in a different k-space line as shown in Figure 8. The

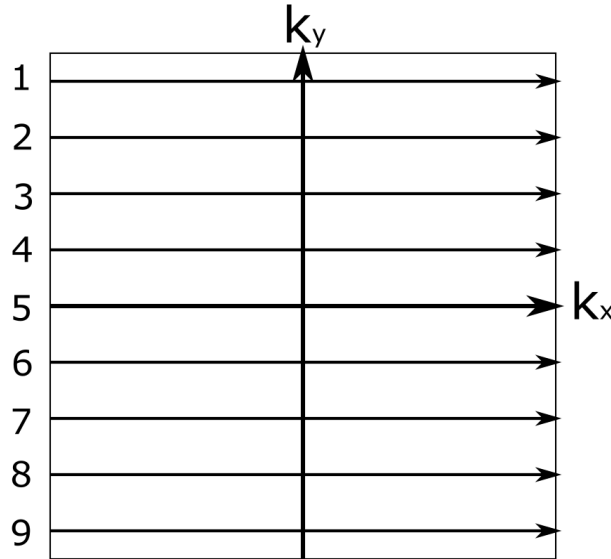


Fig. 8: Cartesian filling of k-space with 9 readouts

number of data points collected in each direction in k-space is called the matrix size. Increasing the matrix size typically increases the scan time and resolution as more data points need to be acquired.

F. Fourier Transform

To obtain an image in the standard spatial domain, a Fourier transform (FT) needs to be performed on the k-space information. The Fourier transform is a mathematical operation that yields the spectral content of a signal [1]. The signal of a 2D sample $s(x,y)$ is acquired as a signal in k-space $S(k_x,k_y)$ following:

$$S(k_x, k_y) = \int_x \int_y s(x, y) e^{-i2\pi(k_x x + k_y y)} dx dy \quad (8)$$

The FT and inverse FT (IFT) can be used to transform back and forth between domain pairs such as (time, frequency) and (image space, k-

space). Therefore, the following IFT can be used to produce an image from k-space information:

$$s(x, y) = \int_{k_x} \int_{k_y} S(k_x, k_y) e^{i2\pi(k_x x + k_y y)} dk_x dk_y \quad (9)$$

In MRI, the sampling process provides a finite number of data points instead of a continuous function and a Discrete Fourier transform [21] (DFT) is used. Typically, an algorithm called a Fast Fourier Transform [22] (FFT) is used for fast and efficient computation of the DFT. The obtained image consists of voxels, with voxel being a 3D unit with a single value with dimensions in x, y and z (analogous to a pixel which is a 2D unit).

G. Radial MRI using an azimuthal increment based on the Golden Ratio

Radial MRI uses radial readouts with equal azimuthal increments to sample k-space, where each readout begins at the edge of k-space, passes through the centre and ends at the other edge as shown in Figure 9. For a given matrix di-

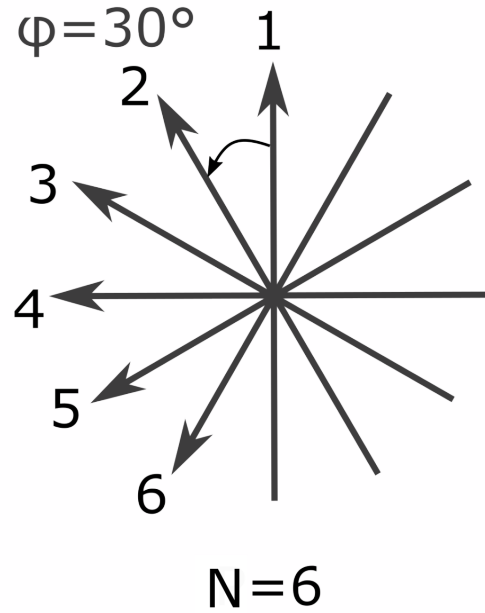


Fig. 9: Radial filling of k-space with number of radial readouts N and azimuthal increment φ .

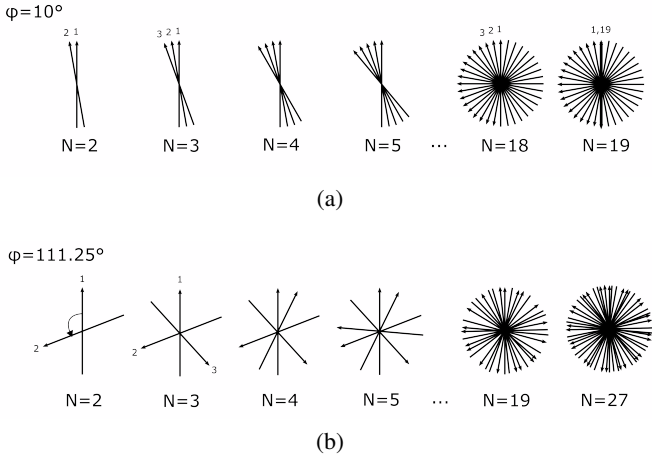


Fig. 10: Radial readouts based on (a) a fixed increment and (b) the golden angle of 111.25° for a given number of readouts N .

ameter d , the number of unique, non-repeating radial readouts required for a fully sampled k-space according to the Nyquist criteria [23] N is given by (equivalent to half the circumference of a circle):

$$N = \pi \cdot \frac{d}{2}. \quad (10)$$

Radial sampling of k-space is often used for dynamic imaging when high temporal resolution is desired, as it is less sensitive to motion artifacts compared to Cartesian sampling [8]. The lower sensitivity to motion artifacts is due to the oversampling of the k-space centre, which preserves the low spatial frequency image information. While undersampling results in streaking artifacts, the low spatial frequency image information, which gives the overall image structure, is preserved due to the oversampling of the k-space center. A uniform readout distribution with a constant azimuthal increment was shown to be optimal when the number of readouts N is predetermined and fixed [8]. This can be seen from Figure 10 (a) as the increment of 10° is optimal only for $N = 18$ readouts. Radial MRI using the golden angle as an azimuthal increment has been demonstrated to

provide a nearly uniform k-space coverage for an arbitrary number of radial readouts [8] as shown in Figure 10 (b). The golden angle has a value of 111.25° and results from:

$$\phi_{GR} = \frac{180^\circ}{\beta} \quad (11)$$

where $\beta = 1.618$ is the Golden Ratio and solves the equation:

$$\beta^2 = \beta + 1 \quad (12)$$

The Golden Ratio was defined by Euclid in his book *Elements* (c. 300 BC), in which he described a finite straight line being cut in such a way that the ratio between the whole line and the greater segment is the same as the ratio between the greater and the lesser segment [24]. When using the golden angle as the azimuthal increment, each subsequent readout divides one of the largest gaps in k-space [8] and avoids sampling the same radial readout twice, unlike the example from Figure 10 (a) for $N = 19$ (where the 1th and 19th readout have the same angular position). A sliding window reconstruction can be used to reconstruct images with flexible temporal resolution by selecting a temporal window width and temporal window shift. During this reconstruction, only the readouts within the window are used to reconstruct a single image as shown in Figure 11. The ability to reconstruct images from windows with an arbitrary width and position, along with the ability to combine readouts from different windows makes the golden angle radial MRI sampling strategy viable for dynamic imaging.

H. Gradient Echo sequence

The gradient echo (GRE) [25] sequence uses a flip angle α , which is typically 90° or smaller, and frequency encoding gradients to dephase and rephase the transverse magnetisation.

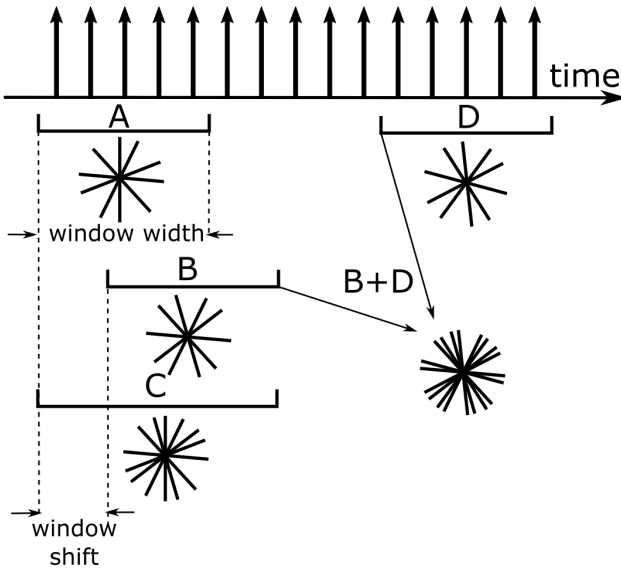


Fig. 11: Sliding window reconstruction shown with windows A and B. It is possible to reconstruct an image using readouts from windows with different widths (A and C) and different positions in time, due to the golden angle increment. Reconstructing an image also becomes possible using readouts from different windows, which do not overlap, such as B and D. This concept is used to achieve CINE reconstructed images.

Rephasing the protons results in a temporary increase in FID signal, as shown in Figure 12, called an echo, during which k-space is acquired using the readout gradient. The figure shows a typical gradient echo sequence diagram with echo time (TE) being the time between the RF pulse and the centre of the gradient echo, and the repetition time (TR) being the time between successive pulse sequences. Small flip angles and short repetition times are used for Fast Low Angle Shot (FLASH) [11] GRE imaging which is typically done to acquire fast GRE images.

I. Multi-slice sequence

A multi-slice 2D sequence consists of the application of multiple RF pulses within one TR to cover more than one slice of the sample. Each pulse is centred at a different frequency and there-

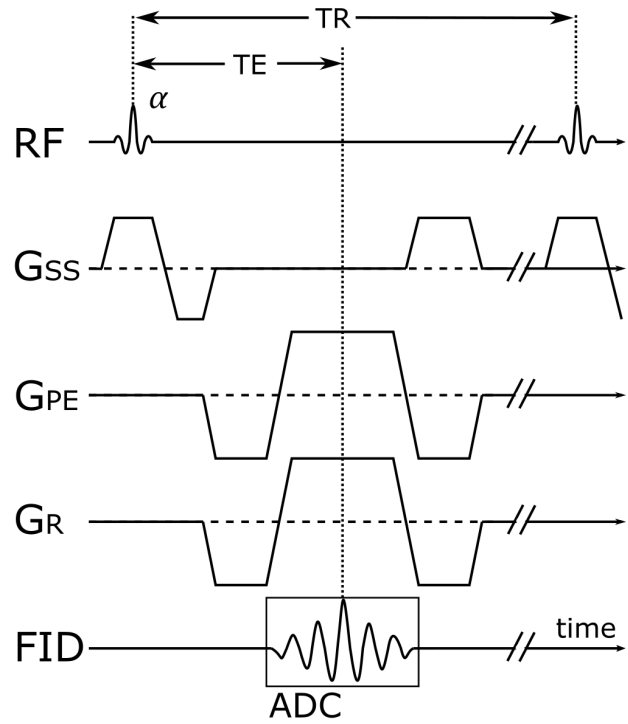


Fig. 12: Typical pulse and gradient sequence used for Gradient Echo acquisitions with radial sampling of k-space. The axes show the RF excitation pulse, slice selection G_{ss}, phase encoding G_{PE} and readout G_R gradients, the FID signal and the analog-to-digital conversion (ADC).

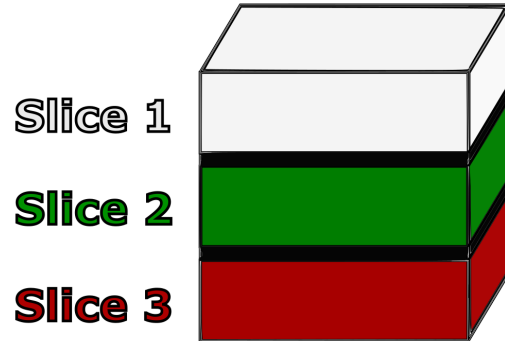


Fig. 13: Sketch of a 3D volume with 3 slices. The slices are separated by gaps shown in black.

fore excites a different slice [2]. Typically, a gap is left between the slices to avoid partial excitation in an adjacent slice from imperfections in the spatial profile of the excited slice caused by the temporally limited duration of the RF pulse. Figure

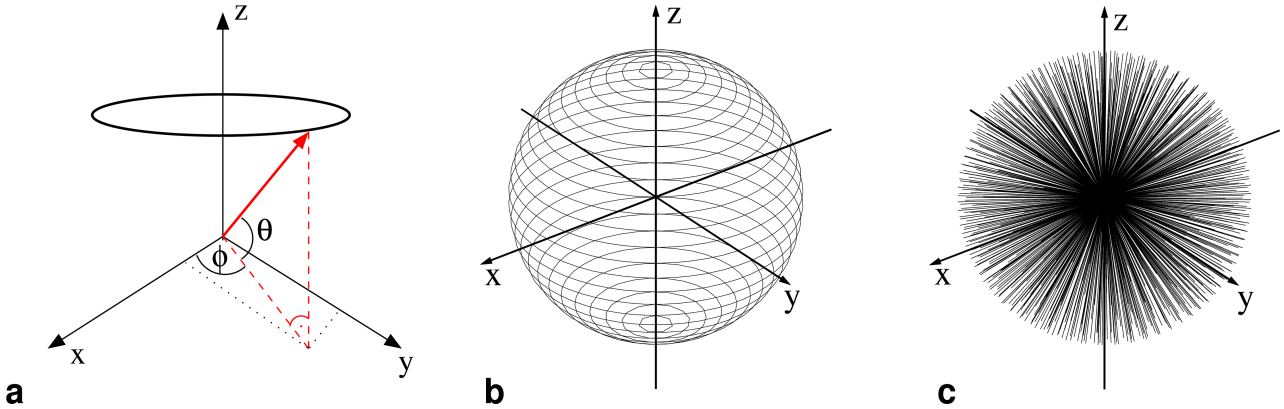


Fig. 14: 3D distribution of readouts in k-space [26]. In (a), the coordinate system for the readouts is defined where each readout starts at the k-space centre and points to different end positions on a circle of constant latitude. Circles of different latitude form a spherical surface (b), resulting in a 3D distribution of readouts (c).

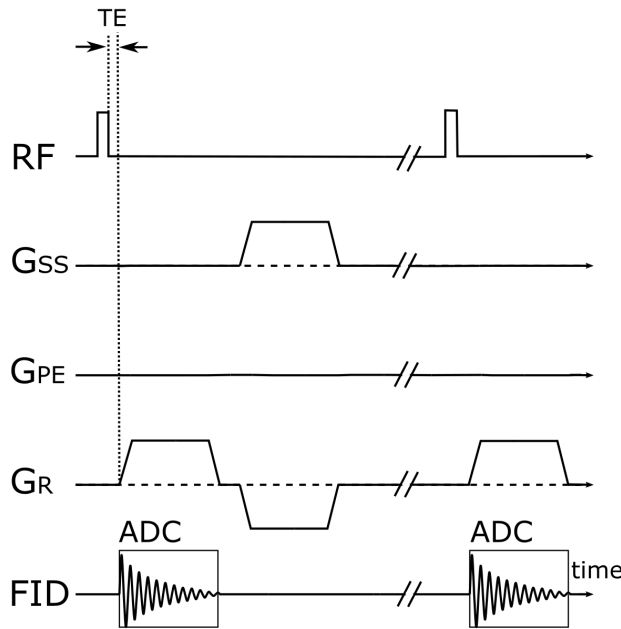


Fig. 15: 3D UTE sequence diagram for radial sampling of k-space. The diagram is shown for acquiring one readout. The readout gradient G_R is rotated in x, y and z to fill k-space according to the distribution shown in Figure 14.

13 shows a volume with 3 slices. In this case, the sequence acquires the first readout for slice 1, slice 2 and slice 3 in that order. Then, the second readout is acquired for the 3 slices in the same order and this follows for all subsequent readouts.

J. 3D UTE sequence

The 3D Ultra short Echo Time (UTE) sequence utilises a short, non-selective RF pulse with a rectangular shape in the time domain, also called a hard pulse. The pulse has a broad enough bandwidth to excite a wide range of frequencies and allows to shorten the echo time substantially. The TE in a UTE sequence is defined as the time between the end of the RF pulse and the start of data acquisition, with typical TE values ranging between 100-250 μ s, although echo times as short as 8 μ s have been reported [27]. A difference between the 3D UTE and the multi-slice sequence is that there is no need for a gap to avoid partial excitation, as a large slab is excited as 3D k-space (shown in Figure 14) that is also encoded in 3D. As shown in Figure 15, data acquisition starts after a short delay between switching on the gradient G_R and the RF pulse to shorten the echo time. Using this sequence, the start and end points of the readouts no longer lie on a circle in k-space, but rather on a spherical surface as shown in Figure 14. The number of unique readouts required for a

fully sampled k-space can be determined by:

$$N = 4\pi \cdot \left(\frac{d}{2}\right)^2 \quad (13)$$

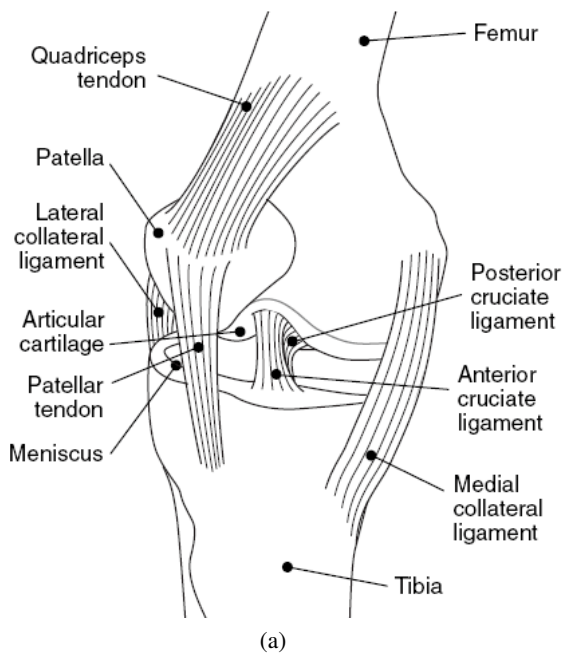
where d is the matrix diameter. As shown in Figure 14, the readouts start from the centre of k-space and traverse it in a circular motion at a constant latitudes. The 3D k-space data is then interpolated to a Cartesian grid prior to the inverse FFT [28].

III. METHODS AND MATERIALS

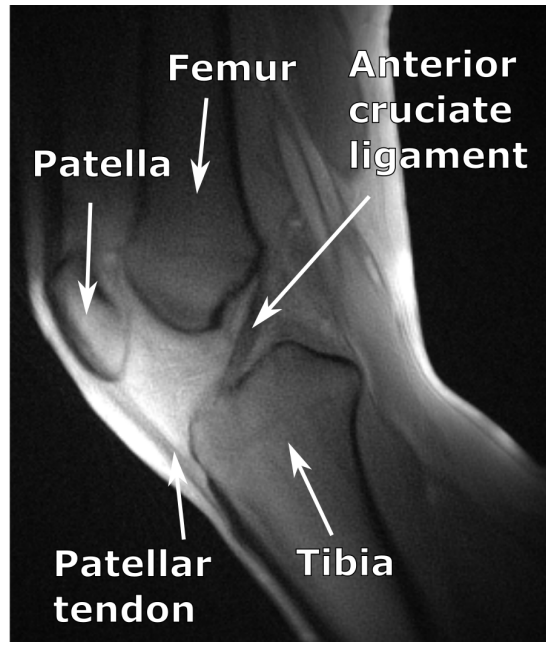
This section provides a description of the knee loading device used during the MR measurements, the method for synchronising the angular position data from the rotary encoder with the MRI data and the different MRI measurements performed with a 3T Siemens Prisma fit scanner. Figure 16 shows anatomical structures of the knee.

A. Description of the Device

The device shown in Figure 17 was designed during a preceding research project funded by the German Research Foundation (DFG DU 298/25-1, RE 1123/22-1) by the Julius Wolff Institute at the Berlin Institute of Health & Charité – Universitätsmedizin Berlin. Its purpose is to allow dynamic imaging of repeatable cycles of knee flexion-extension. The device is positioned such that half of the device is inside the MR scanner, supported by the inner railings that guide the patient table and the other half rests on the patient table and is secured to it by a number of pins. Inside the bore of the MR scanner, the device allows for a range of motion approximately up to 40°. The front part consists of a platform on which weights can be placed for additional resistance and a gear system that translates the movement of the knee to the platform via a roller chain. The weights are MRI safe, being made from a plastic housing and filled with sand. With the subject lying supine,



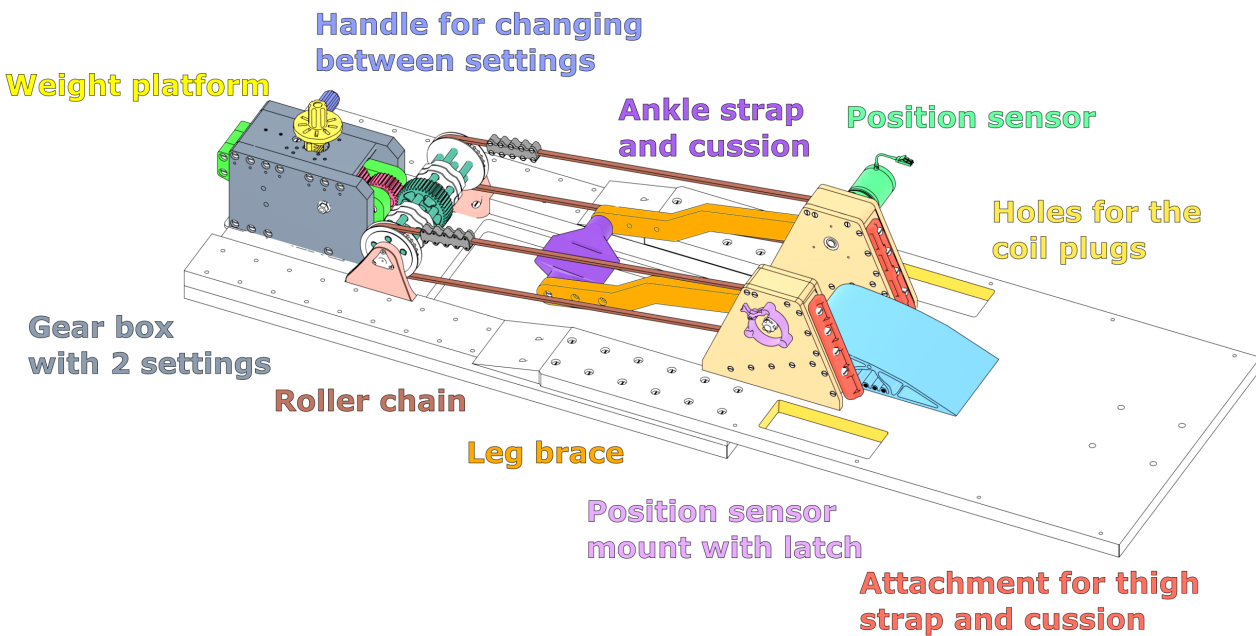
(a)



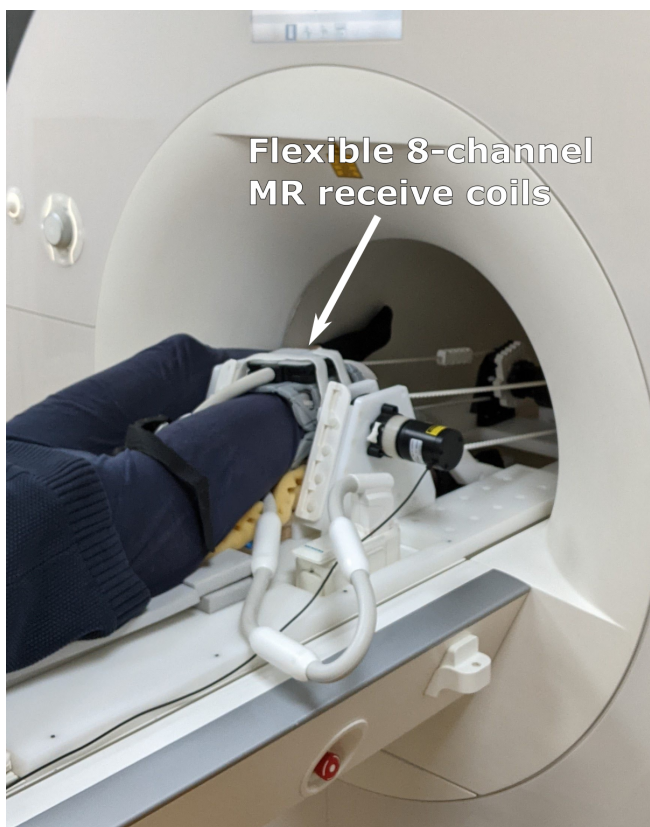
(b)

Fig. 16: Diagram (a) and high resolution image (b) of the knee with labeled anatomical structures.

the platform has 2 settings - one for pushing the load up and one for pulling it down. Settings can be switched by removing the violet handle from the gear box shown in Figure 17 and moving the green block (seen at the end of the gear box) either up or down. Once a setting has been chosen, the handle



(a)



(b)



(c)

Fig. 17: Sketch (a) and photos (b) and (c) of the device with labeled components. The front part, with the weight platform, goes into the bore of the scanner first as shown in (c), and the rear part is where the subject lays and fits their leg through the leg brace, and where two MR receive coils are placed below and above the knee as shown in (b). Sandbags are placed under the subject's left leg for comfort.

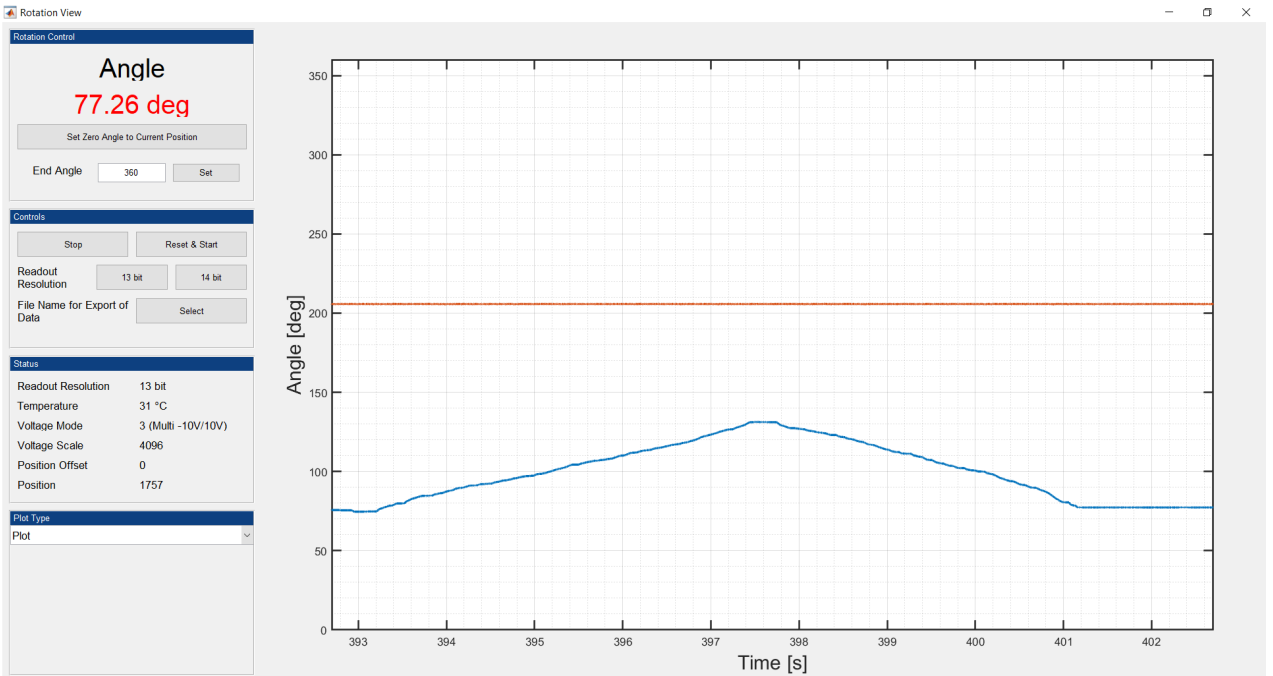


Fig. 18: The Graphical User Interface used to record data. The red horizontal line shows the trigger signal from the MRI scanner, which is a constant value when there is no trigger pulse. The blue line shows the digitised signal from the rotary encoder and corresponds to the red value of the angle top left. The specific values of the lines are not significant, as the recorded data is normalized prior to synchronisation. The image shown was not captured during measurement. Here, the sensor was rotated only for demonstration.

is placed back. The rear part of the device is where the subject lays and places their knee on wooden blocks and cushions to elevate it to a position where the centre of rotation of the joint (i.e., the pivot point) is aligned with the centre of rotation of a leg brace. In the sketch shown in Figure 17, these blocks and cushions are represented by the blue platform. Two flexible 8-channel MR receive coils are secured with straps, with one being below and the other above the knee. A strap immobilizes the leg above the knee to minimize movement, and the foot goes above or below the leg brace, depending on the movement being performed (pushing or pulling). The longitudinal position of the leg brace cushion can be adjusted using screws, depending on the length of the subject.

An MR338 ZapFREE fiber optic absolute position sensor (<https://micronor.com/product/mr338/>)

(also referred to as rotary encoder in this work) from Micronor is placed in the mount on either side of the device, as shown in Figure 17 and a small white latch locks it in place. The sensor is MRI safe, immune to electromagnetic fields, and measures absolute angular position from 0° to 360° with a resolution of 0.025°. An MR330-1 controller module from Micronor (<https://micronor.com/product/mr330/>) outside the MRI area (i.e., the MRI examination room) is connected to the sensor and outputs the rotation angle as voltage. A RedLab 1208FS-PLUS Universal Serial Bus (USB) Data Acquisition (DAQ) module from Meilhaus Electronic (<https://www.meilhaus.de/en/redlab-1208.htm>) is used to digitise the voltage signal and outputs it to a computer via USB. Connected to the RedLab

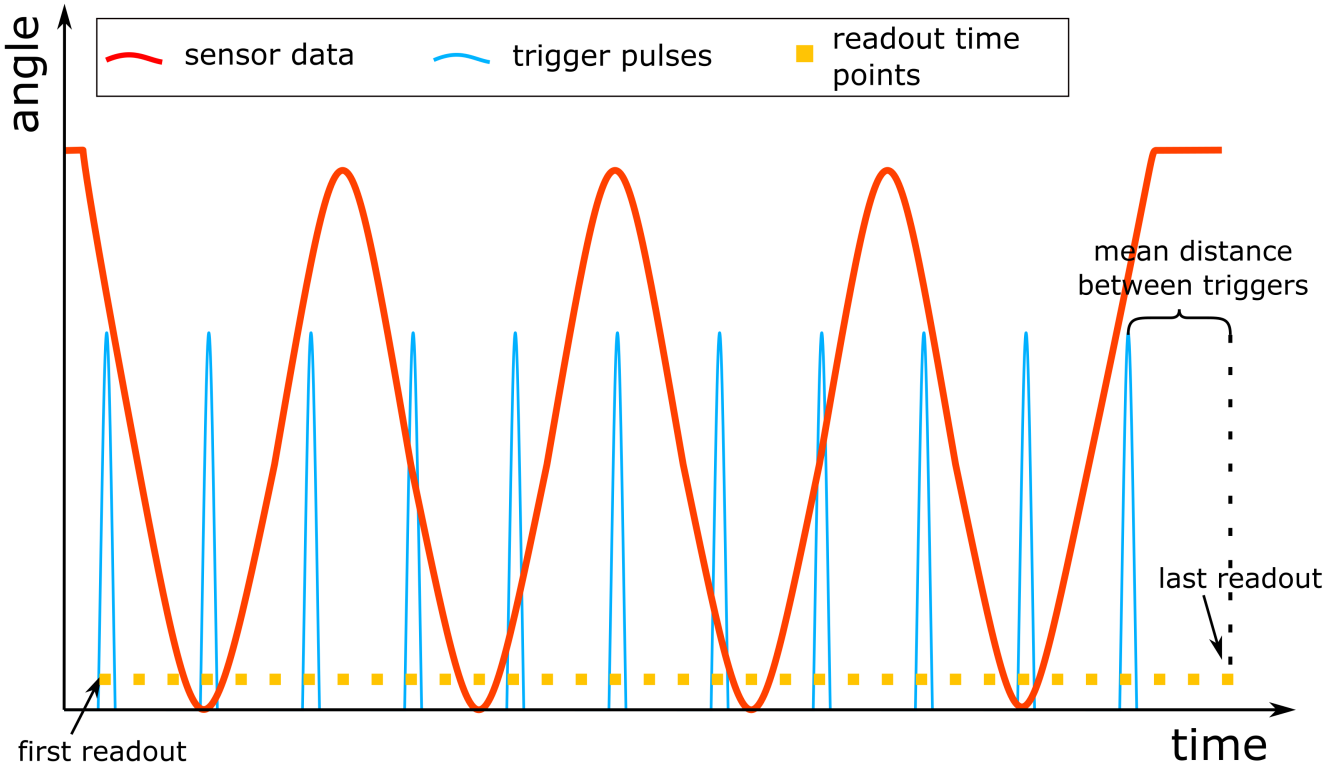


Fig. 19: Illustration of the rotary encoder data (red) and trigger pulses (blue), that are stored using the Graphic User Interface from Figure 18. The yellow points are the calculated time points at which radial readouts were recorded (it is worth noting that they have no angle value and are displayed above the time axis for visualisation purposes).

module is a cable that comes from a custom-built conversion box that converts the optical trigger signal from the MRI scanner into an electrical signal. This short voltage trigger pulse has a duration of 10 ms and comes as output at the start of a readout acquisition in k-space. Once k-space is fully sampled according to equation (10), the process of filling k-space is repeated with a trigger pulse at the start of each sequence repetition. A custom MATLAB script runs the graphic user interface, as shown in Figure 18, that can be used to record and save the digitised rotary encoder and trigger signal data. The stored data file contains the time in milliseconds, the digitised sensor data and the digitised trigger signal as one-dimensional lists.

B. Data synchronisation and reconstruction

Figure 19 illustrates how the rotary encoder and trigger data look like after normalisation of the saved data file from the GUI shown in Figure 18. For clarification regarding the former figure, motion characterised by a decreasing angle represents concentric motion during extension and an increasing angle represents eccentric motion during flexion. As shown in blue in Figures 19 and 20, there is only 1 trigger pulse at the beginning of each sequence repetition and a predetermined number of radial readouts N between the triggers shown in yellow. Synchronising the rotary encoder data with the MRI data (i.e., the acquired radial readouts) is crucial for reconstructing knee images at a specific angular position and for CINE, as

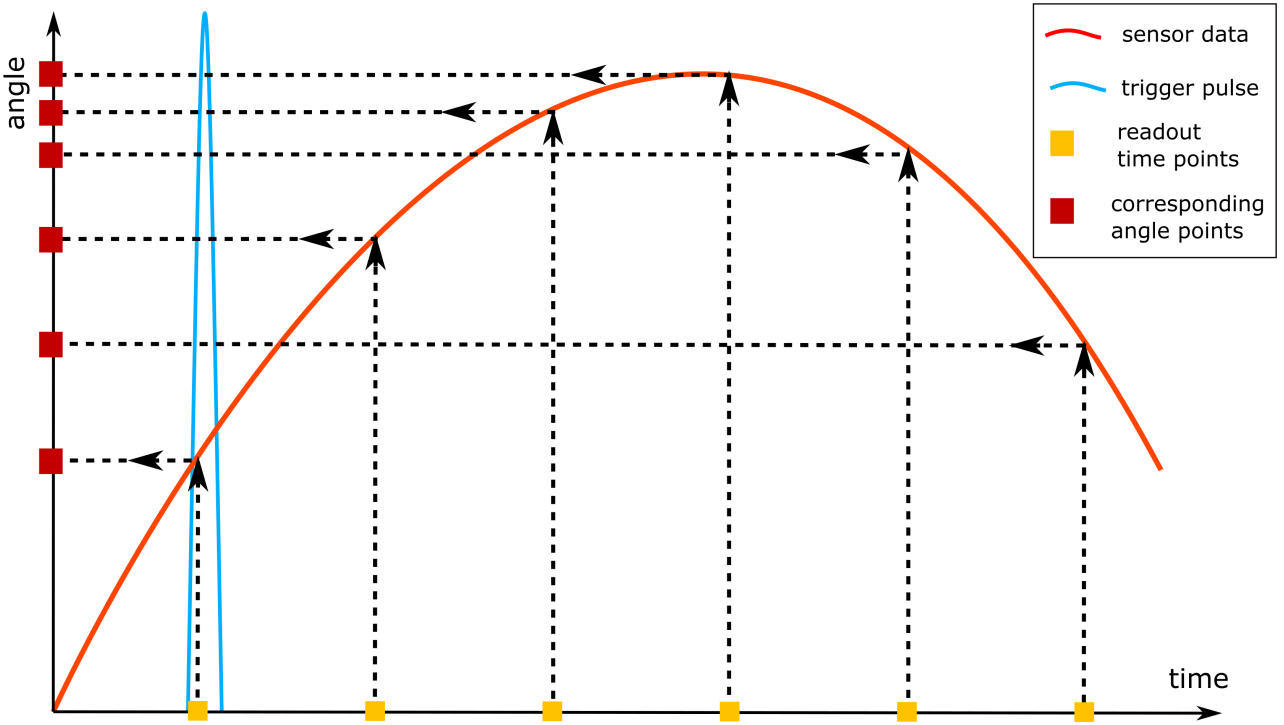


Fig. 20: Illustration of how the rotary encoder and radial readouts are synchronised. The yellow points represent the time at which a readout is acquired and the result are points that have both an angle value and a time value, making it possible to identify at which angular position the leg was for each radial readout.

the radial readouts used for CINE reconstruction need to have been acquired during the same phase of motion. The synchronisation was a three step process involving identification of the trigger pulse timestamps, calculating the timestamps of all acquired readouts during measurement and finding the nearest time values between the acquired readouts and the rotary encoder data. Firstly, the full width at half maximum was used to find the timestamp of the rising flank of each trigger pulse. The rising flank is used to reduce any trigger pulse shape inconsistencies resulting from electrical conversion of the optical trigger signal. In addition, the mean difference in time between the rising flank timestamps was determined to approximate the time taken for a single repetition. Secondly, a linear array of time points was created with a

start and an end point, as shown in Figure 19 by the first and last readout. Additionally, the total number readouts acquired during the total MR scan (usually comprising several motion cycles) is used to fill the time between the start and end points with equally spaced time points. The start point is the first rising flank, representing the time the first radial readout was acquired. The last rising flank does not indicate the last radial readout, as there are N readouts following that trigger pulse that would not be accounted for. To correctly calculate the end point, it is required to sum the timestamp of the last rising flank with the mean difference between rising flank timestamps which accounts for the last N readouts. These two points are the first and last recorded readout. The total number of timestamps is the number of readouts per repetition

multiplied by the number of repetitions.

Figure 20 shows a sketch that illustrates the concept of synchronisation. Before synchronisation, the readouts shown in yellow only have time values. Finally, finding the nearest time values between the rotary encoder data and the radial readout timestamps results in the angle values of the knee at which each readout was acquired. These corresponding angle values are shown as red dots in Figure 20, which is only used for illustration.

Image reconstruction was a two-step process. Firstly, the readouts for a specified angle \pm a specified range of angles (referred to as angle window) of the synchronised data were found (see Figure 21), and a list of their indices was created. Secondly, images were reconstructed using readouts given by these indices, resulting in an image of the knee at the chosen angular position.

In this work, two methods were used to reconstruct images depending on which indices, and therefore readouts, were selected based on the synchronised data. For indices selected for a specific angle and angle window from a single flexion-extension Motion Cycle (MC), we refer to real-time reconstruction as shown in Figure 21. Analogously, when indices were selected from more than one motion cycle, we refer to as CINE reconstruction.

Figure 22 shows the differences in signal between images reconstructed during flexion and extension, respectively. The difference in signal is likely due to physiological changes in muscle tissue during concentric and eccentric motion [29]. Reconstructing an image using readouts acquired during both flexion and extension would therefore result in blur due to the signal difference shown in Figure 23.

A general practice adopted in this work was

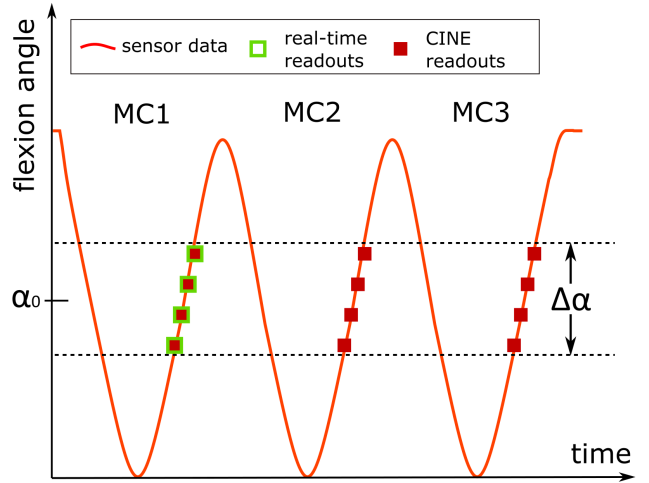


Fig. 21: Illustration of how readouts are selected for a specified angle α_0 and angle window $\Delta\alpha$ during knee extension. For the real-time reconstruction, only the points outlined in green would be used, while all points in red would be used for CINE reconstruction.

to select readouts acquired during knee flexion (as shown in Figure 21) for image reconstruction, for consistency. Another general practice adopted concerns the signal from the two 8-channel receive coils used. In some cases, a single or multiple channels could result in a substantially stronger signal in the reconstructed image due to close contact with the skin as shown in Figure 24 (a). In the event of images having such signals, the corresponding channels were identified by reconstructing the images again without channel combination. The identified channels were then reduced on a case by case basis prior to the inverse FFT and the images were reconstructed again with channel combination. The signal of the identified channels was typically reduced by 50%. This process was done to obtain images that would be visually easier to interpret as shown in Figure 24 (b). The change in intensity would not affect efforts in morphological analysis (such as tissue thickness or volume) or T_1 and T_2 fitting, which would be done



Fig. 22: CINE image reconstructed with readouts acquired during extension overlaid with its absolute difference image (in red) with a CINE image reconstructed with readouts acquired during flexion.



Fig. 23: CINE image (zoomed in) reconstructed with readouts acquired during flexion (left), extension (middle) and both flexion and extension (right).

voxel by voxel over an additional echo dimension.

C. Measurements

The following measurements were conducted with a 3T Siemens Prisma fit scanner. The subjects involved in the measurements were a 28-year-old

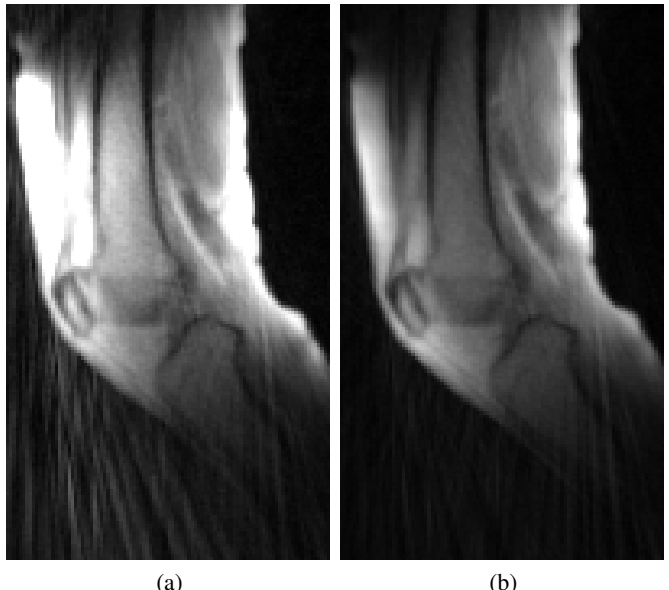


Fig. 24: Real-time reconstructed images without (a) and with (b) signal reduction from receive coil channels that are in close contact with the leg.

female and a 24-year-old male. They were positioned supine, feet first and strapped in the device with the knee flexion-extension plane aligned with the sagittal plane. Two 8-channel flexible coils were placed below and above the knee of the subject. Since the device allows the addition of weights, two 5 kg weight plates and two 1.5 kg sandbags were placed onto the weight platform of the device, to increase the resistance on the leg. The same weight was used for all measurements described below, unless stated otherwise. Different pulse sequences and sequence parameters were used during measurements. For this reason, measurement protocols are defined below and will be referred to throughout the section.

Protocol I: recording a single 2D slice of the knee using a golden angle radial MRI sequence [12] with sequence parameters $\text{TE/TR} = 2.43/5.10$ ms, voxel size = $1.5 \times 1.5 \times 4.8 \text{ mm}^3$, matrix size = 144×144 with a flip angle of 10° and 226 radial readouts per repetition. Repetition refers to

one application of the sequence, which is repeated multiple times during a measurement. The number of repetitions is stated separately for each measurement, as some measurements used a different number of repetitions to decrease the overall acquisition duration and reduce the strain on the subjects. Regarding the sequence of the golden angle, the different radial positions for the 226 readouts of a single repetition were identical for all subsequent repetitions.

Protocol II: recording a single high resolution 2D sagittal slice of the knee using the golden angle radial MRI sequence (GA) with sequence parameters TE/TR = 2.43/7.0 ms, voxel size = $0.7 \times 0.7 \times 3.0 \text{ mm}^3$, matrix size = 320×320 with a flip angle of 10° and 502 radial readouts per repetitions.

Protocol III: recording a single 2D sagittal slice of the knee using the golden angle radial MRI sequence with sequence parameters TE/TR = 2.43/7.0 ms, voxel size = $1.3 \times 1.3 \times 7.2 \text{ mm}^3$, matrix size = 176×176 with a flip angle of 18° and 276 radial readouts per repetition.

Protocol IV: recording a single 2D sagittal slice of the knee using a continuous golden angle radial MRI sequence (CGA) with sequence parameters TE/TR = 2.43/7.0 ms, voxel size = $1.3 \times 1.3 \times 7.2 \text{ mm}^3$, matrix size = 176×176 with a flip angle of 18° and 276 radial readouts per repetition.

Protocol V: recording six 2D sagittal slices of the knee using a continuous golden angle radial MRI sequence with sequence parameters TE/TR = 2.43/32 ms, voxel size = $1.3 \times 1.3 \times 3.6 \text{ mm}^3$, matrix size = 176×176 with a flip angle of 18° and 276 radial readouts per repetition.

Protocol VI: recording a 3D slab of the knee using a 3D UTE sequence with sequence parameters TE/TR = 0.03/1.3 ms, voxel size = $2.1 \times 2.1 \times 4.4 \text{ mm}^3$, matrix size = $96 \times 80 \times 18$ with a flip angle

of 4° and 9176 radial readouts per repetition. This sequence does not use the golden angle as an azimuthal increment due to challenges in implementation for a non-isotropic 3D k-space.

To illustrate the possibility of reconstructing images at different angular positions of the leg, a measurement with a single sagittal slice through the knee was performed on the 28-year-old female subject, using Protocol I with 200 repetitions and an overall acquisition duration of 4 minutes. During the scan, the subject moved their leg through flexion-extension motion cycles to the beat of a metronome set to 30 bpm, with a change in motion (from flexion to extension and vice versa) taking place every 8 seconds. The time it took to complete one flexion-extension motion cycle was therefore 16 seconds (16 s/cycle) and approximately 14-15 motion cycles could be completed in the acquisition duration of 4 minutes. Images were reconstructed using the real-time (RT) method for angular positions 30° , 25° , 20° and 15° with angle windows (AW) 1° , 2° , 3° and 5° based on the rotary encoder data shown in Figure 19. To demonstrate the feasibility of CINE reconstruction, images were also reconstructed with the CINE method for the same angular positions mentioned above and angle windows 1° and 2° . Image reconstruction could be performed for other angular positions within the range of motion and for other angle windows. For consistency, the angular position of 25° and the angle window of 2° were chosen as reconstruction parameters for all following image reconstructions unless stated otherwise.

A reconstructed image could suffer from undersampling artifacts such as streaking or blurring if its k-space is not fully sampled. Knowing the extent to which k-space is sampled (i.e., the number of radial readouts with unique radial positions) for the aforementioned reconstructed images could

therefore give insight on why one image suffers more/less from undersampling artifacts compared to the others. To find the extent of k-space sampling for each reconstructed image, the number of unique radial readouts used for each reconstructed image was determined and the number of unique radial readouts required for a fully sampled k-space was calculated using equation (10). Dividing the former number by the latter results in a percentage of sampled k-space.

In the aforementioned measurement, the subject performed one flexion-extension motion cycle every 16 seconds. However, motion of the knee joint during daily activities is typically performed at a higher speed (such as standing up, walking, jumping, etc.). Conducting MR measurements of flexion-extension motion cycles with a faster moving leg is therefore of interest to capturing more physiological motion and musculoskeletal mechanics. It is then a question if and how higher leg motion speed affects CINE reconstructed images. Two additional measurements with a sagittal slice through the knee were performed using Protocol I on the 28-year-old subject. One measurement was performed with 100 repetitions and the other with 80 repetitions, with the metronome set to 60 bpm (8 s/cycle) and 90 bpm (5.3 s/cycle) respectively. The acquisition duration of both scans was approximately 2 minutes. The number of repetitions for the measurements was changed to keep the number of flexion-extension cycles the subject had to perform approximately the same (the subject performed approximately 14 motion cycles for both the 30 bpm and 60 bpm measurements and 17 motion cycles for the 90 bpm measurement). CINE images were reconstructed from the 30 bpm, 60 bpm and 90 bpm measurements, with readouts acquired during the first 80 repetitions, for consistency. The number of unique radial readouts

was calculated for each reconstructed image to compare the extent of k-space sampling.

All following measurements were performed with a metronome tempo set at 60 bpm unless stated otherwise. This tempo was chosen to avoid muscle fatigue in the subject, due to the duration of the conducted MR measurement sessions being approximately 1-1.5 hours.

Higher resolution knee images could improve morphological analysis of a moving knee, such as measuring tissue thickness, due to the edges of the tissues being sharper. To demonstrate CINE reconstructed images for high resolution data, a measurement with a sagittal slice through the knee was performed on the 24-year-old subject using Protocol II with 65 repetitions and overall acquisition duration of 4 minutes. CINE images were reconstructed with angle windows 1°, 2°, 3° and 4° to observe the effect of the angle window on the high resolution images.

In theory, it would be possible to reconstruct an image with high spatial resolution from a longer measurement where the subject moved their leg through many more flexion-extension cycles. In practice, however, any leg motion that is not flexion or extension could result in a shift in the leg position in the device. To check for possible lateral movement and to investigate reproducibility, 5 measurements with a transverse slice through the femur bone were taken in both subjects in separate sessions and on different days. The measurements were carried out using Protocol I with 200 repetitions and overall acquisition duration of 4 minutes. Analysis was performed by reconstructing real-time images during extension and during flexion with readouts from each flexion-extension motion cycle. This resulted in a total of 10 data sets, 5 sets of reconstructed images during flexion and 5 sets of reconstructed images during extension.

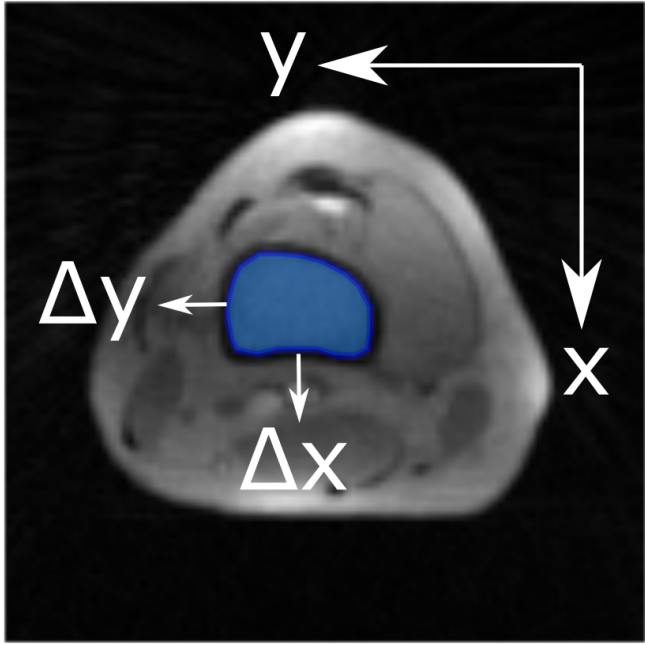


Fig. 25: Real-time reconstructed image from a transverse slice through the femur with a drawn region-of-interest drawn around the femur. Once the ROI is copied onto another real-time reconstructed frame and aligned with the femur bone, the ROI centre of mass will have a shift Δx and Δy in the x- and y-directions respectively.

The following process was performed on each of the 10 data sets. A region-of-interest (ROI) was drawn around the bone as shown in Figure 25 for a single frame and was translated manually to match the position of the bone in all the other frames. Bicubic interpolation with a factor of 3 was used on the images to allow a sub-pixel accuracy of the drawn ROI as shown in Figure 26. It is worth noting that the region-of-interest was copied from one frame to another in each data set, keeping it the same shape and not altering it in any way other than translation. The centre of mass of the regions-of-interest for each frame was calculated in the x- and y-directions for each of the 10 data sets. The centre of mass values in both x- and y-direction for the first frame were subtracted from all the calculated values, in the respective data set,

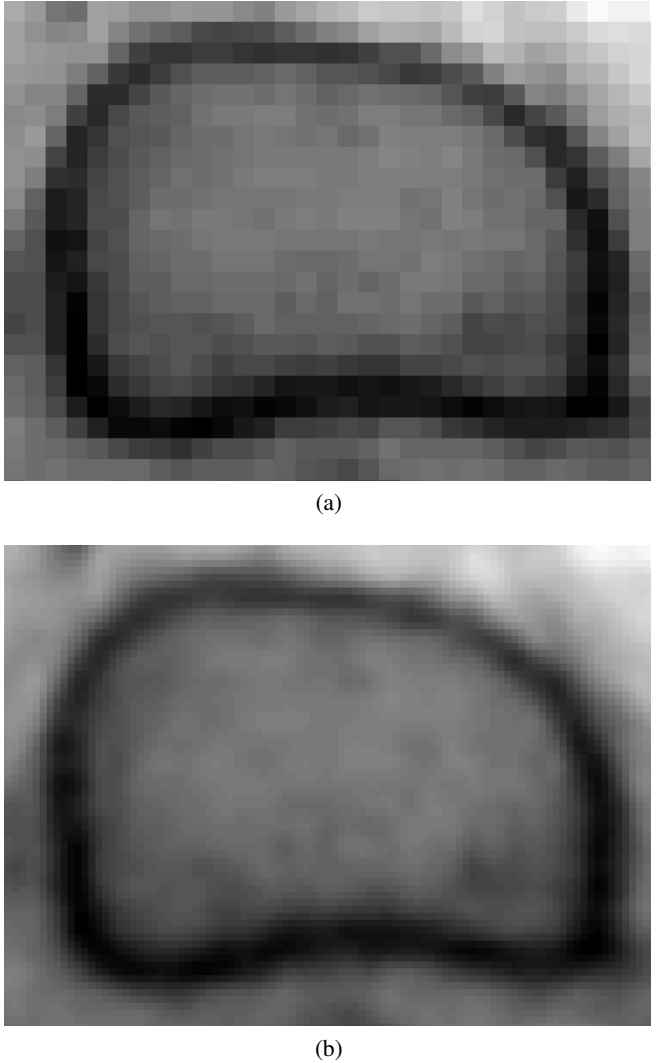


Fig. 26: Zoomed in image of the femur bone from the transverse scan of Figure 25 before (a) and after (b) using bicubic interpolation with factor 3.

to obtain the shift in x- and y-direction (Δx and Δy) of the ROI from frame to frame. Thus, the shift for the first frame would always be zero as it is the reference. Standard deviation of the shifts in each direction (x and y) was calculated for each of the 10 data sets to find how big the fluctuations in the shifts are.

To check for possible motion in the sagittal plane, analysis was performed on the sagittal slice data with metronome speeds 30 bpm, 60 bpm and 90 bpm by reconstructing real-time images during extension and during flexion for each flexion-

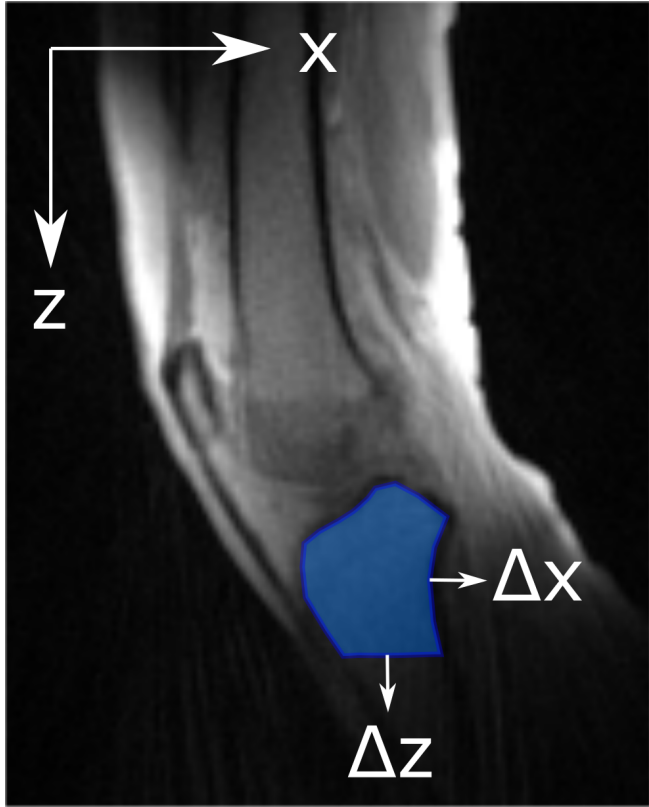


Fig. 27: Real-time reconstructed image from a sagittal slice through the knee with drawn regions-of-interest around the tibia bone.

extension cycle. This resulted in a total of 6 data sets of reconstructed images, 3 sets during flexion and 3 sets during extension. Regions-of-interest were drawn for the tibia bone for each of the 6 data sets, as shown in Figure 27, for one frame and translated manually to match the bone in all other frames. The centre of mass of the ROIs was calculated in the x- and z-directions for each data set with the value for the first frame subtracted from all values to obtain the shift Δx and Δz from frame to frame. Standard deviation of the shifts in the sagittal plane were calculated for each of the 6 data sets in each direction (x and z) to find how big the fluctuations in the shifts are.

The golden angle sequence uses identical radial readout positions for each sequence repetition. This suggests there could be readouts used for

CINE reconstruction and real-time reconstruction (in case of a large angle window) with repeating radial positions. This is a potential hindrance to practical applications as more repetitions (and therefore a longer overall acquisition durations) are necessary to fully sample the k-space of a given image compared to a protocol or sequence (such as the continuous golden angle) that does not use repeated readout positions. Comparing CINE reconstructed images from a golden angle and a continuous golden angle sequence would therefore give insight on whether using only unique radial readout positions reduces the number of repetitions necessary for a fully sampled k-space and whether such a sequence has potential drawbacks. To compare the k-space sampling of these two sequences, one measurement was performed with Protocol III (GA) and the other with Protocol IV (CGA) for 50 repetitions and an overall acquisition duration of 2 minutes.

The GA measurement resets the angle of the radial readout to zero at the start of each repetition, such that the same 276 radial readout positions are used for 50 repetitions. In contrast, the CGA measurement does not reset the angle, resulting in 13800 (276×50) unique readout positions. Figure 28 shows the result of combining readouts from two repetitions acquired by a GA and CGA sequence. Analysis was performed by calculating the number of unique radial readouts of a CINE reconstructed image from each measurement for angular position of 25° and angle window of 2° , and for a different number of repetitions, namely from 1 to 50.

Practical applications such as segmentation of the whole knee require a larger spatial coverage, which can be achieved using multi-slice (MS) and 3D UTE sequences. Using data from dynamic MR measurements to reconstruct real-time images is

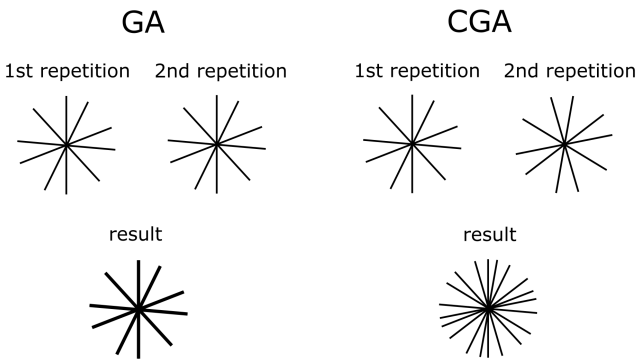


Fig. 28: Golden Angle (GA) and Continuous Golden Angle (CGA) readout acquisition for 2 repetitions with 5 radial readouts each. GA uses the same readout positions for each repetition by resetting the angle at the start of each repetition, whereas CGA does not reset the angle and avoids repeating positions. The result of combining the readouts from both repetitions is a k-space with 5 unique readout positions for the GA and 10 unique readout positions for the CGA.

likely to result in strong undersampling artifacts due to the low number of unique radial readouts. However, CINE reconstruction includes an overall higher number of readouts and the resulting images are expected to suffer from fewer artifacts. For larger spatial coverage of the knee, a sagittal multi-slice measurement was performed on the 24-year-old subject and two 3D UTE measurements were performed on the 28-year-old subject. The MS measurement was conducted using Protocol V with 35 repetitions and overall acquisition duration of 5 minutes. Images were reconstructed using real-time and CINE methods for the 25° angular position, with angle window 2° . The number of unique radial readouts was calculated for the CINE image to find the extent of k-space sampling.

3D UTE is useful to morphological analysis not only because of its larger spatial coverage of the knee, but also because of its ability to detect signals from tissues with a short T_2 value such as tendons and ligaments. The anterior cruciate

ligament in Figure 16, for example, appears dark from the signal decay. The patellar tendon in the figure appears bright due to the magic angle effect [30], which occurs when collagen tissues such as the tendon are oriented at a specific range of angles in relation to the static B_0 field, and will appear dark for other angular positions outside of this range. The k-space filling for 3D UTE takes a long time compared to golden angle the sequences used thus far. For this reason, it can be expected that some areas of k-space may not be filled while selecting readouts with the angle window. Gaps in k-space could result in image artifacts and finding a way to minimise gaps could significantly improve the reconstructed images. By altering the readout orientation during acquisition, the CINE reconstructed images could have a more evenly filled k-space. Two 3D UTE measurements were performed with Protocol VI for 22 repetitions and acquisition duration of 4 minutes, using two different techniques for 3D k-space filling. The measurements were conducted without weights for the comfort of the subject, due to the long measurement session. One measurement was without segmentation, in which the k-space readouts are recorded in succession. The other measurement was with a segmentation factor of 32, such that a readout with an initial orientation is recorded in k-space, after which the position jumps 32 steps and the next readout is recorded, as shown in Figure 29. CINE images were reconstructed for each of the two 3D UTE measurements and the number of unique radial readouts was calculated to find the extent of k-space sampling.

To demonstrate a potential application for musculoskeletal analysis using CINE reconstructed images, a measurement with metronome speed of 30 bpm (16 s/cycle) was performed with Protocol I for 200 repetitions and overall acquisition duration

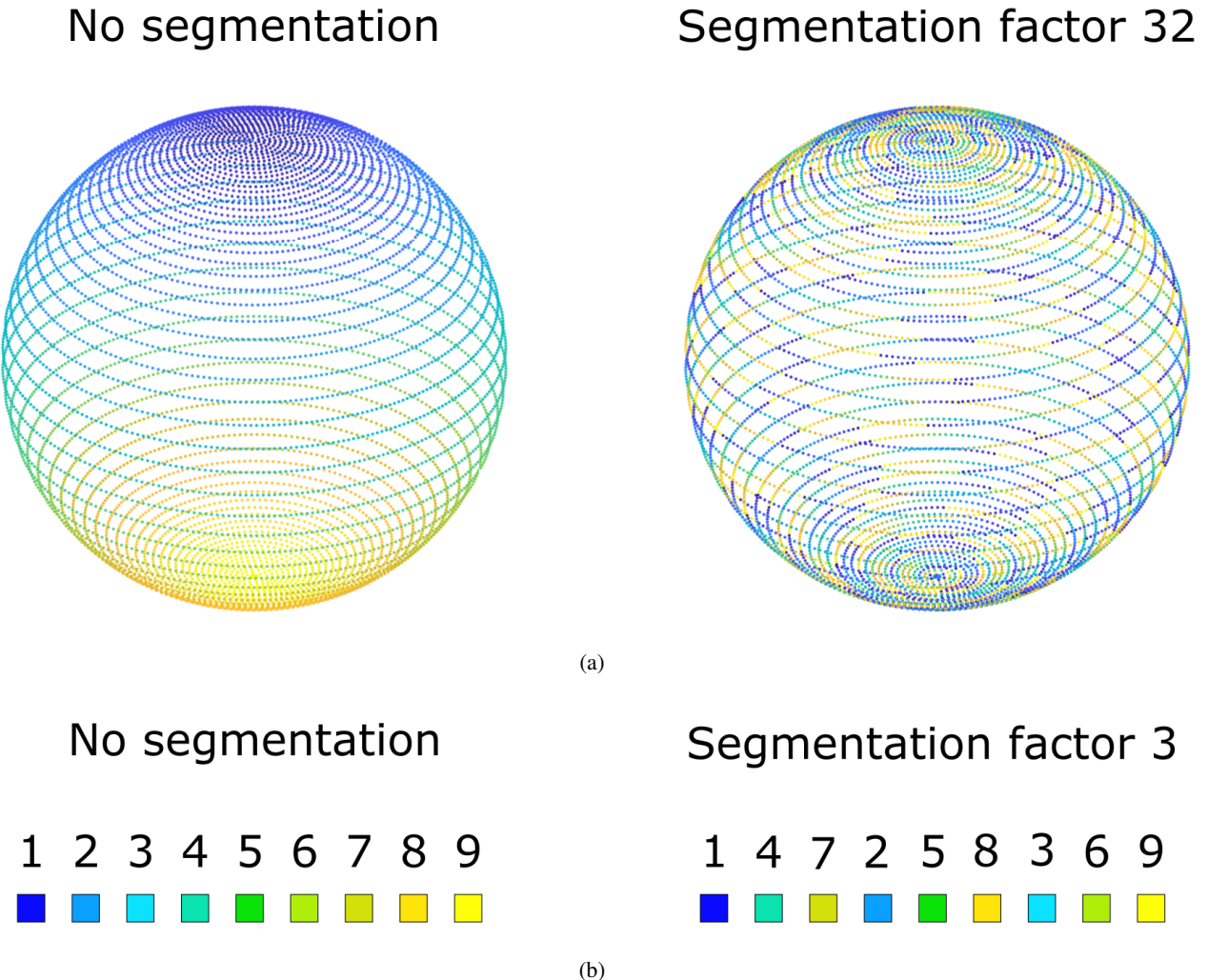


Fig. 29: K-space filling for 3D UTE without segmentation and with segmentation factor 32 (a). A 1D line with 9 readouts without segmentation and with segmentation factor 3 (b) is included to illustrate the concept for a simpler scenario.

of 4 minutes on the 28-year-old female subject, with the weights removed. This measurement was carried out during the same session with the same subject as the 30 bpm measurement (with weight) described at the beginning of this section. CINE images were reconstructed from both 30 bpm measurements (with and without weights) and were aligned. To align the images, firstly, a region-of-interest was drawn around the tibia bone for one image (with weights) and was copied and translated to fit the tibia bone of the second image (without weights). Secondly, using the difference

in x and z positions of the centre of mass of the ROIs, the second image was translated such that the two regions-of-interest of the images were in the same position. Thirdly, with the tibia bones in the two images aligned, an absolute difference image between the two was calculated. Finally, the first image was overlaid with the absolute difference image to observe the differences in signal between the with and without weight images.

IV. RESULTS

A. Real-time and CINE images from the 30 bpm measurement with weight

Figure 30 shows the rotary encoder data of the 30 bpm (weight) measurement with the synchronised points used for real-time and CINE reconstruction. The rising flanks of the trigger pulses were used to calculate the timestamps of the radial readouts. The standard deviation of the distance between trigger pulse rising flanks was calculated to be $\sigma = 0.5 \text{ ms}$, with mean distance $d = 1153 \text{ ms}$. This standard deviation suggests

that the timestamps of the radial readouts are sufficiently approximated. As can be seen from the 1st flexion-extension motion cycle in Figure 30, labelled MC1, the subject's motion performance can result in inconsistencies in the motion curve. Other inconsistencies are the upper and lower limits of the range of motion, as seen from MC4 and MC5 in the figure.

Figure 31 shows real-time (RT) and CINE reconstructed images with a 2° angle window for 4 different angular positions based on the rotary encoder data shown in Figure 30. It can be seen

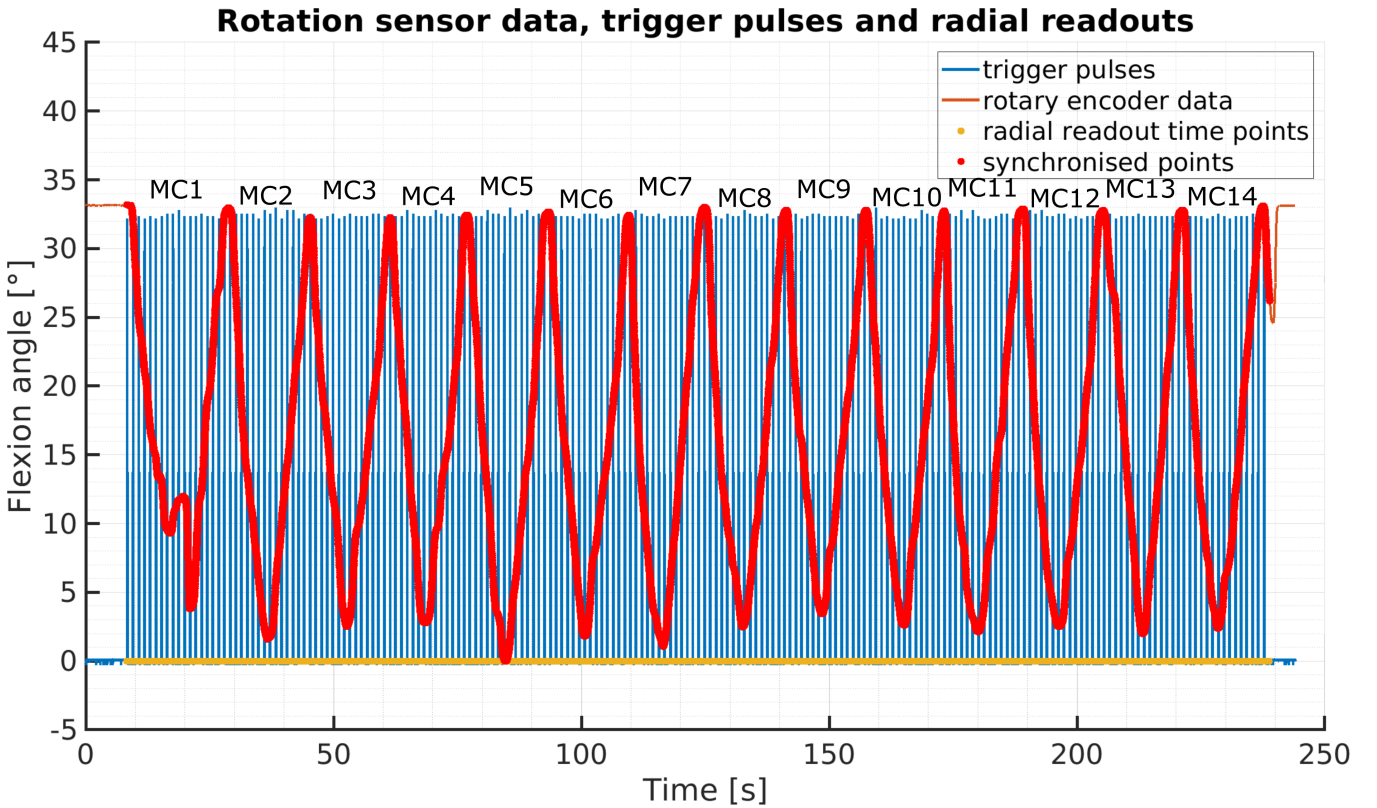
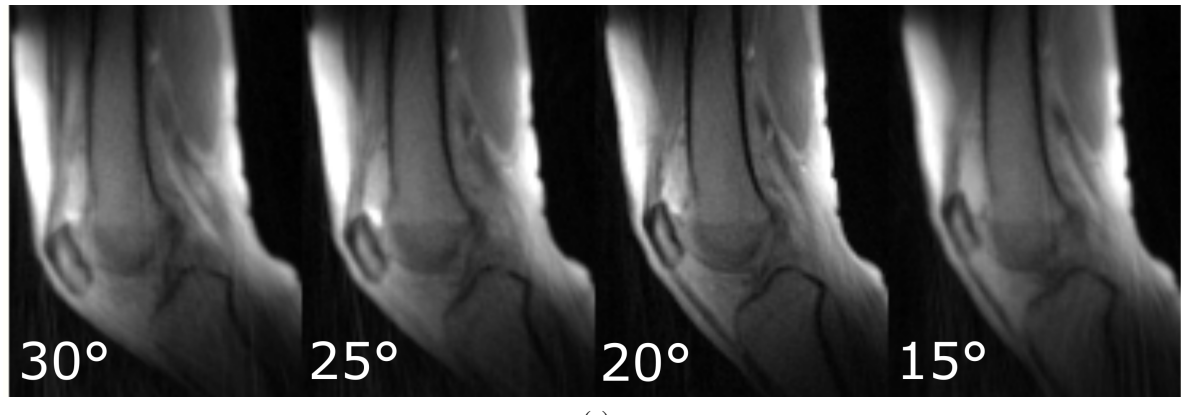
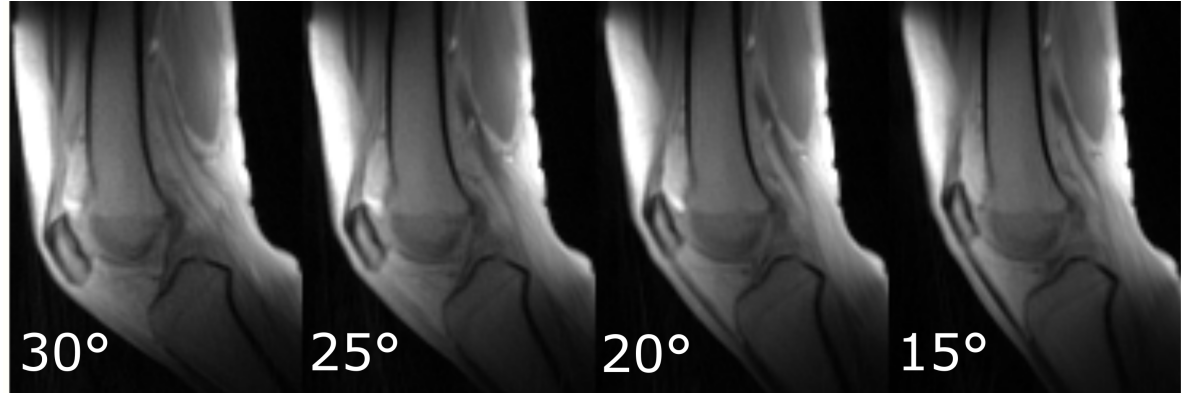


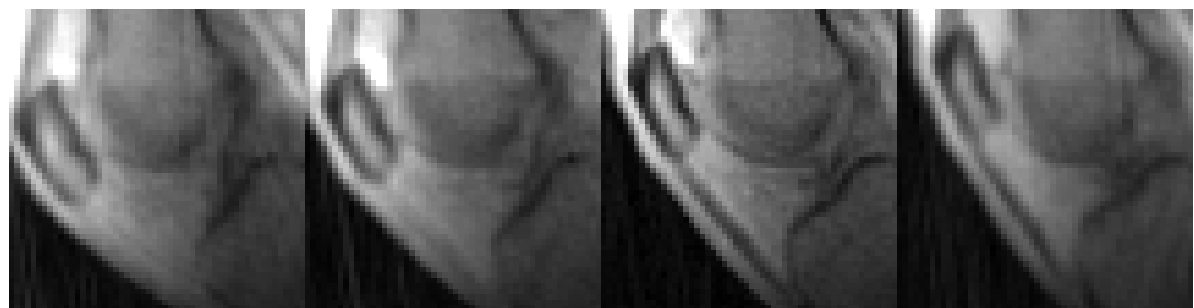
Fig. 30: Rotary encoder data, trigger pulses with synchronised points for the 30 bpm measurement with weights. Due to the trigger pulse duration of 10 ms, small variations in duration can result in the blue lines appearing thicker or thinner. This, however, has no practical significance in the context of image reconstruction. The rotary encoder data has been normalized such that the zero represents full extension of the leg. What appears as a horizontal yellow line is in fact 45200 yellow time points representing time at which radial readouts were recorded. The thin red line, largely overlapped by the synchronised points, is the angular position signal coming from the encoder, smoothed with a Savitzky–Golay filter. The 14 flexion-extension motion cycles (MC) shown in the rotary data are given labels from MC1 to MC14.



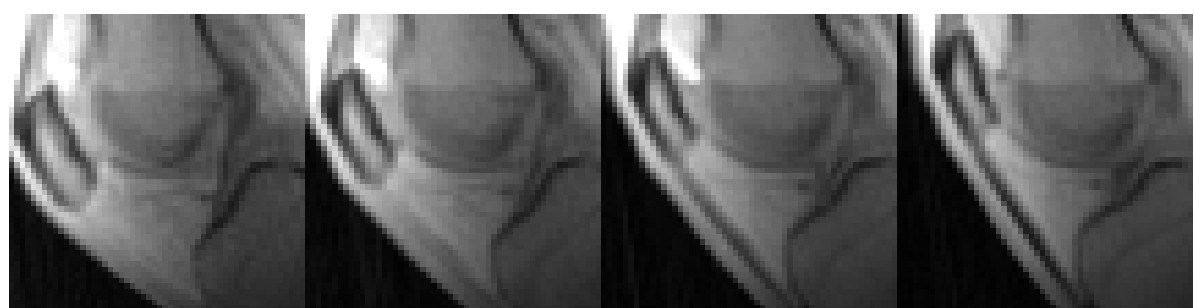
(a)



(b)



(c)



(d)

Fig. 31: Real-time (a) and CINE (b) reconstructed images with an angle window of 2° for 4 angular positions based on the rotary encoder data. The real-time images were reconstructed from radial readouts acquired during the first motion cycle (MC1) shown in Figure 19. The real-time and CINE images are shown as zoomed in versions in (c) and (d) respectively.

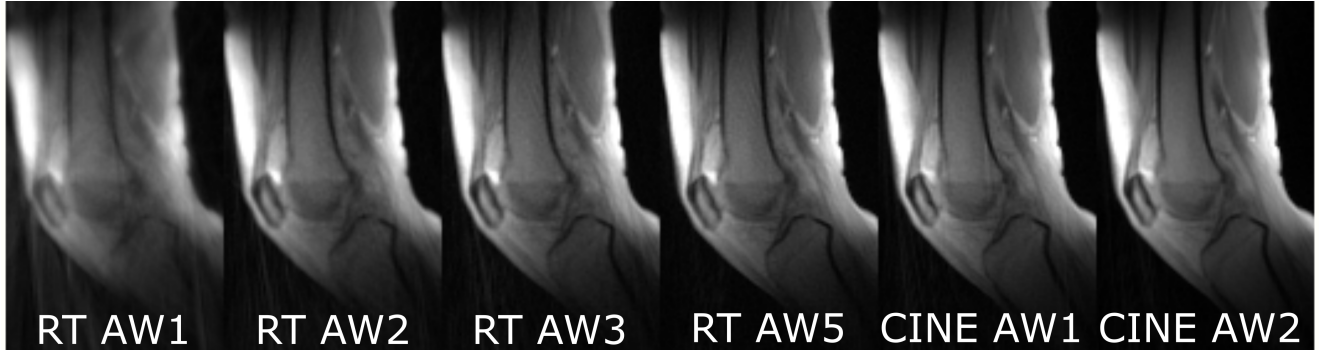
that synchronising the rotary encoder and MRI data allows for the reconstruction of CINE images using radial readouts from multiple flexion-extension cycles. Visually comparing the images, the CINE reconstructed images overall suffer from less streaking and undersampling artifacts. The CINE images also appear sharper than the RT images, due to the larger number of radial readouts (from more flexion-extension motion cycles) used in reconstruction. From visual assessment, the 20° RT image could be argued to have comparable quality to the 20° CINE image. This is likely due to the subject moving slower at this particular angular position compared to the RT images shown for angular positions 30° , 25° and 15° , thereby allowing for more readouts to be acquired for that RT image. However, the larger readout number for the 20° RT image results from inconsistencies in subject motion. Such inconsistencies will result in RT images being reconstructed with a substantially different number of radial readouts, preventing comparison of RT images from different measurements and physiological analysis. The CINE reconstructed images in the figure, in comparison to the RT reconstructed images, have an overall more consistent and better quality in terms of visual assessment, and show better promise for practical applications such as measuring tissue thickness.

Figure 32 shows both real-time (RT) and CINE reconstructed images with different angle windows

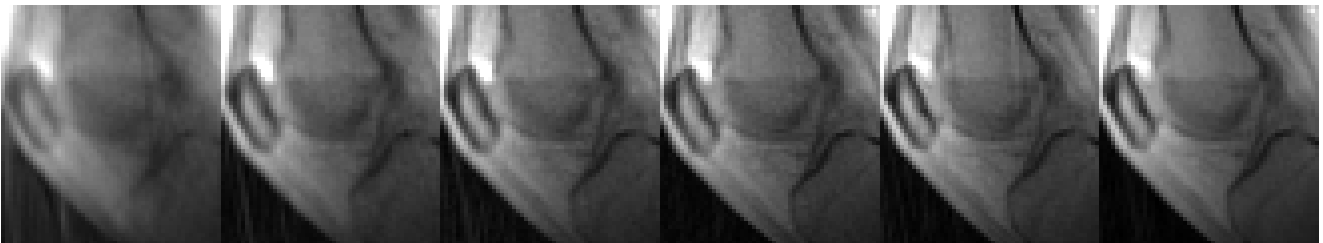
(AW) for the 25° angular position. As can be seen from the real-time images, a smaller angle window such as 1° results in an image with streaking artifacts and poor spatial resolution, due to the percentage of k-space sampling which is listed in Table 1. Increasing the angle window parameter to 2° or 3° includes more unique readouts in the RT reconstruction, resulting in better spatial resolution as can be seen from the RT AW2 and RT AW3 images in the figure. However, a larger angle window includes more radial readouts acquired when the leg is in different angular positions, thus reducing the angular position precision (APP) and how useful that image is for analysis of physiological motion. The two CINE reconstructed images shown in the figure demonstrate higher spatial resolution compared to the RT AW1, RT AW2 and RT AW3 images. For cases where the real-time images have a fully sampled k-space such as the RT AW5 image, the CINE images offer better APP, due to being reconstructed with readouts from a smaller angle window. This shows that CINE reconstruction can be used to produce images with better overall spatial resolution and APP from dynamic MRI data. The two CINE images have 92.5% and 100% sampled k-space, as shown in Table 1. While a smaller angle window is preferred for a better angular position precision, more flexion-extension motion cycles during measurement would be required to reconstruct a fully

Reconstruction	RT AW 1	RT AW 2	RT AW 3	RT AW 5	CINE AW 1	CINE AW 2
Number of readouts	31	68	116	284	469	973
Number of unique readouts	31	68	116	226	209	226
Percentage sampled	13.7%	30.1%	51.3.7%	100.0%	92.5%	100.0%

Table 1: Number of calculated unique radial readouts and the percentage of sampled k-space for the real-time (RT) and CINE reconstructed images from a single slice 2D radial golden angle measurement shown in Figure 32.



(a)



(b)

Fig. 32: Real-time (RT) and CINE reconstructed images from a single slice 2D radial golden angle measurement, with different angle windows (AW) for the 25° angular position. The number of unique radial readouts and the percentage of k-space sampling can be seen in Table 1. A zoomed in version of the images is shown in (b).

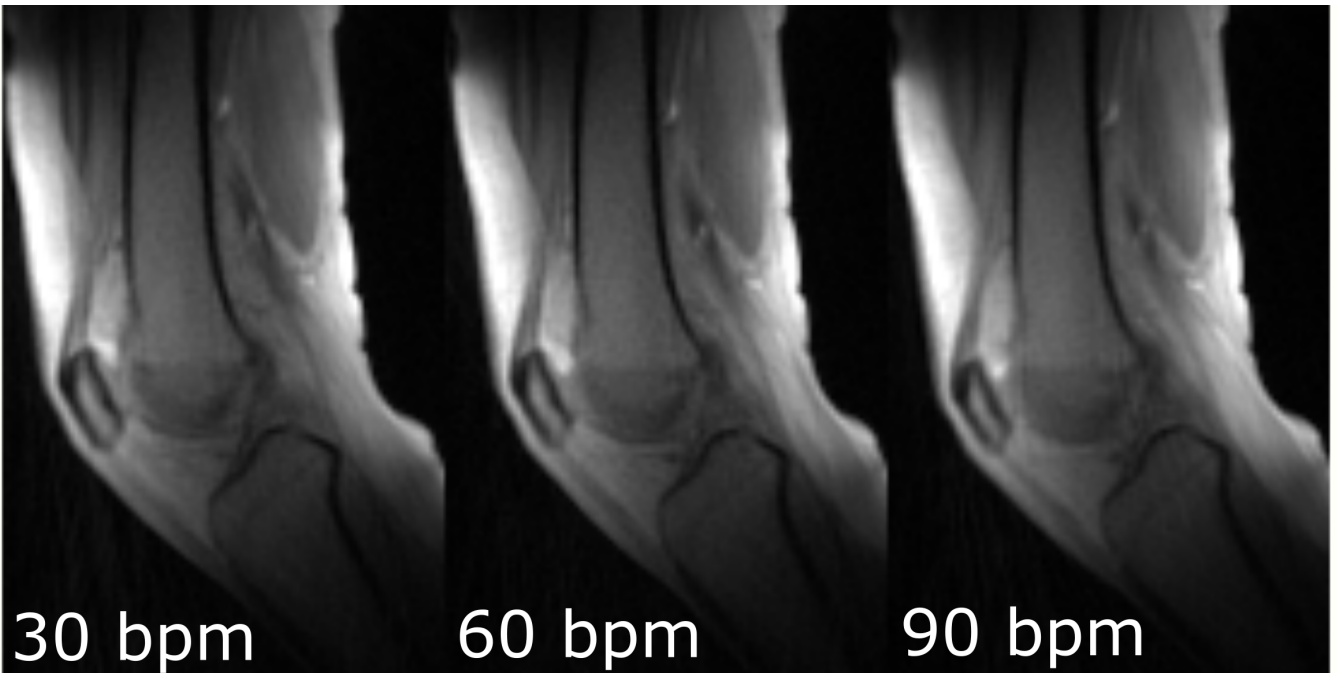


Fig. 33: CINE reconstructed images from 3 sagittal data sets, with different motion speeds with an angle window of 2° for the 25° angular position based on the rotary encoder data. While the measurements were performed with a different number of repetitions, the images shown in this figure were reconstructed using data acquired from the first 80 repetitions, for consistency and comparability.

Reconstruction	CINE 30bpm	CINE 60bpm	CINE 90bpm
Number of readouts	973	611	616
Number of unique readouts	184	211	217
Percentage sampled	81.4%	93.4%	96.0%

Table 2: Number of calculated unique radial readouts and the percentage of sampled k-space for CINE images from three sagittal measurements with different motion speeds shown in Figure 33.

sampled image, thus increasing measurement time. Therefore, the selection of an angle window for reconstruction depends on the desired image characteristics depending on the intended application.

B. CINE images for 3 measurements with different motion speed

Figure 33 shows the CINE reconstructed images for the 30 bpm, 60 bpm and 90 bpm measurements for the 25° angular position. Visual assessment of the images suggests that increasing the speed of the leg motion does not have a significant negative impact on the image quality. From Table 2 it can be seen that the image from the 90 bpm measurement has a higher level of k-space sampling compared

to the 30 bpm and 60 bpm images. This is likely a consequence of the leg moving through a higher number of motion cycles compared to the 30 bpm and 60 bpm measurements, since the speed of the leg motion is the only difference between the three images.

C. High resolution CINE images

Figure 34 depicts CINE reconstructed images from the high resolution measurement for different angle windows. Increasing the angle window parameter primarily affects the angular position precision as shown in the AW4 image, particularly around the patella and tibia where the blurring is noticeable. Overall, the high resolution CINE

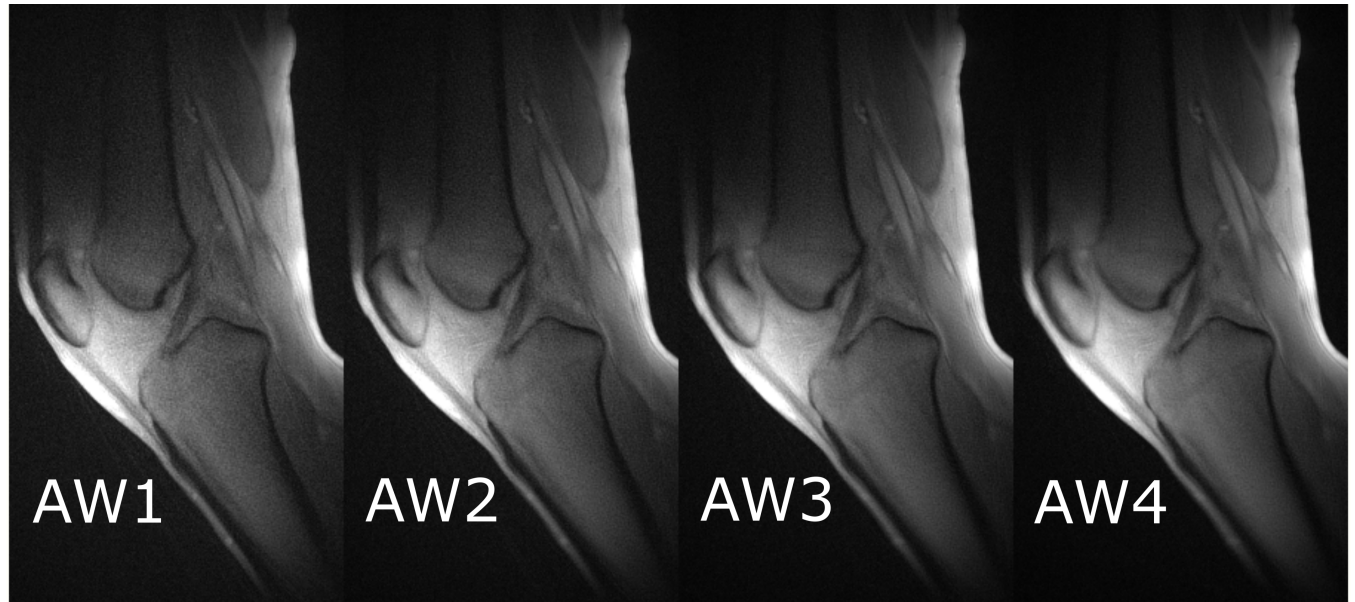


Fig. 34: CINE reconstructed images from the high resolution measurement, with angle windows (AW) 1°, 2°, 3° and 4° for the 25° angular position.

images visually appear sharper than the CINE images shown in Figures 31, 32 and 33 and show potential in being used for morphological analysis such as measuring tissue thickness.

D. Transverse and sagittal shifts of the leg

Figure 35 shows the shift in x (solid lines) and y (dashed lines) direction for the regions-of-interest of the femur bone from the real-time reconstructed images (during extension and flexion) from the 5 transverse measurements. As it can be seen from the figure, the shifts in the y-direction is in the range of 2.5 voxels and 4 mm, and in the x-direction is in the range of 1.3 voxels and 2 mm. This suggests that the device secures the leg only to a limited extent. One consequence of the shifts in the y-direction is that the sagittal slice through the knee during measurements will not be in the same position and a CINE reconstructed image will therefore suffer from effects, such as blurring. Similar blurring is also a consequence of the shifts in the x-direction, due to the leg position in sagittal slices being different across flexion-extension motion cycles. Table 3 shows the standard deviation for each line in Figure 35. It can be seen that the standard deviation for the shifts in the x-direction are overall lower than those in the y-direction, suggesting the motion of the leg in the y-direction is larger than the motion in the x-direction. In the device setup shown in Figure 17, motion in the x-direction (shown in Figure 25) is physically limited by the platform and cushions the leg rests on, and the thigh strap. The aforementioned platform is solid and the leg cannot physically move lower than the top of the platform. Therefore, the compression of the cushions and the thigh strap likely contribute to the extent of the shifts in the x-direction. The cushions could be compressed differently as the

subject performs different flexion-extension motion cycles thus contributing to the shifts in the x-direction. The thigh strap is secured not to the bottom of the device, such that it prohibits the leg moving up, but rather secured at an angle as shown in Figure 17 thereby not restricting motion effectively. This is likely the biggest contributor to the extent of the shifts in x-direction from a device setup standpoint. In the y-direction, there is likely free space available for sideways motion, which could be limited by adding padding or cushions.

Extension

Data	1	2	3	4	5	mean
σ_x [voxel]	0.30	0.26	0.26	0.23	0.22	0.25
σ_y [voxel]	0.52	0.65	0.43	0.54	0.70	0.57

Flexion						
Data	1	2	3	4	5	mean
σ_x [voxel]	0.34	0.32	0.19	0.24	0.22	0.26
σ_y [voxel]	0.51	0.80	0.53	0.34	0.62	0.56

Table 3: Standard deviation σ of the region-of-interest centre of mass shift in x and y, shown in Figure 35, for real-time reconstructed images from five transverse measurements.

Extension

Data	30bpm	60bpm	90bpm	mean
σ_x [voxel]	0.32	0.46	0.46	0.41
σ_z [voxel]	0.33	0.25	0.25	0.28

Flexion				
Data	30bpm	60bpm	90bpm	mean
σ_x [voxel]	0.39	0.34	0.36	0.36
σ_z [voxel]	0.39	0.36	0.38	0.38

Table 4: Standard deviation σ of the region-of-interest centre of mass shift in x and z, shown in Figure 36, for real-time reconstructed images from three sagittal measurements.

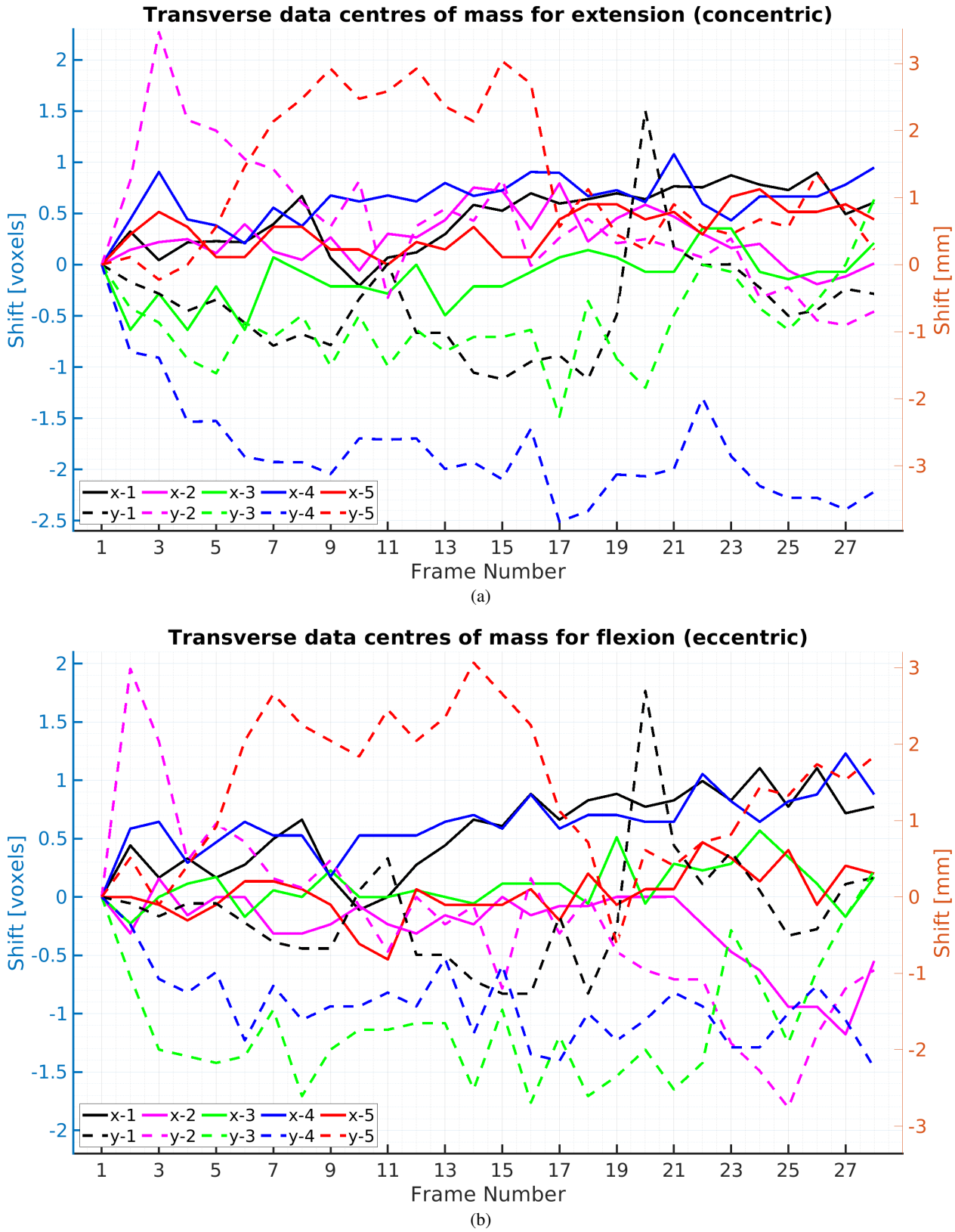


Fig. 35: Region-of-interest centre of mass shift in the x- and y-direction for real-time reconstructed images of the same leg angular position (for different motion cycles) from 5 transverse measurements. Plots (a) and (b) are shown for extension (or concentric motion) and flexion (or eccentric motion), respectively.

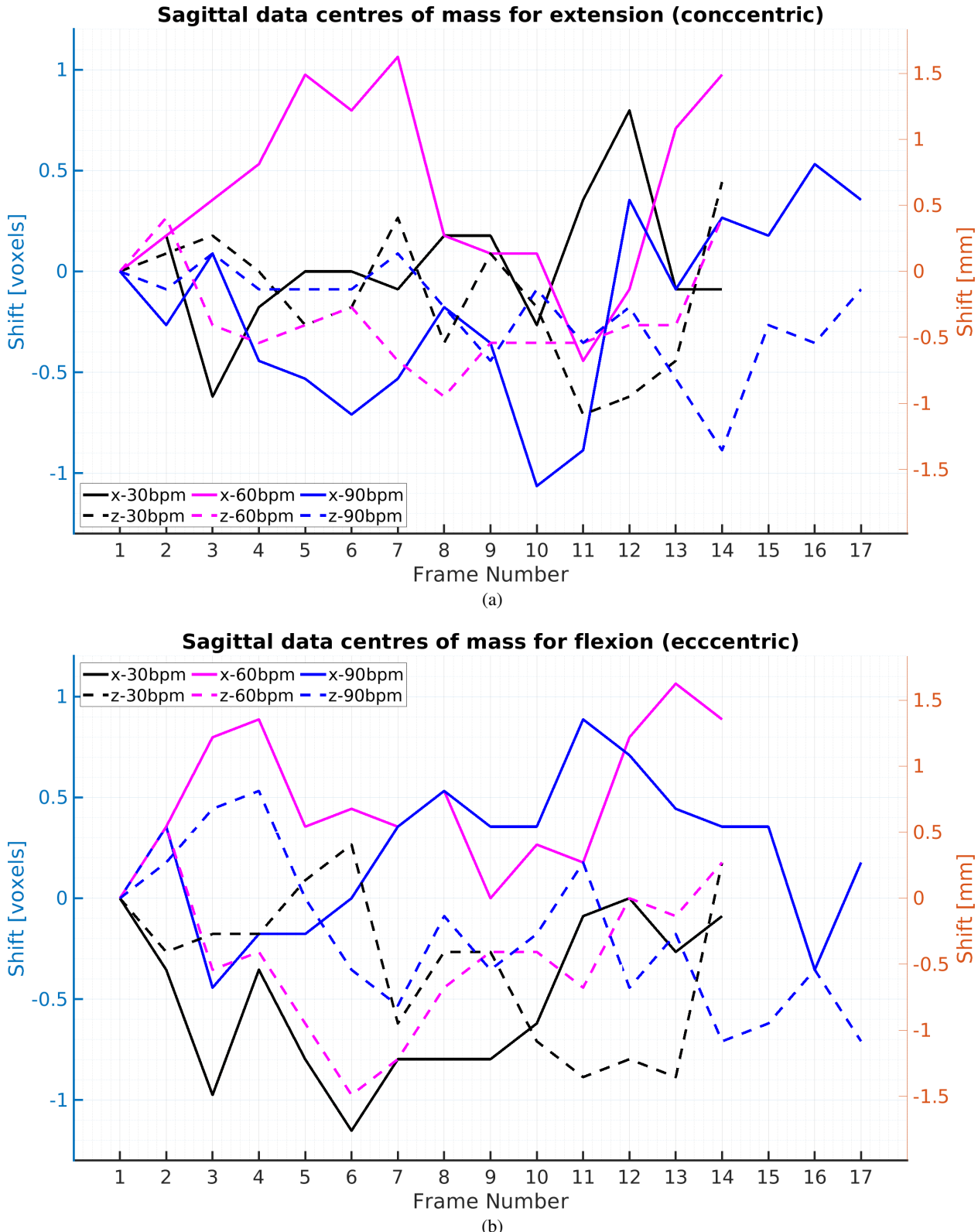


Fig. 36: Region-of-interest centre of mass shift in the x- and z-direction for real-time reconstructed images of the same leg angular position (for different motion cycles) from 3 sagittal measurements. Plots (a) and (b) are shown for extension (or concentric motion) and flexion (or eccentric motion), respectively.

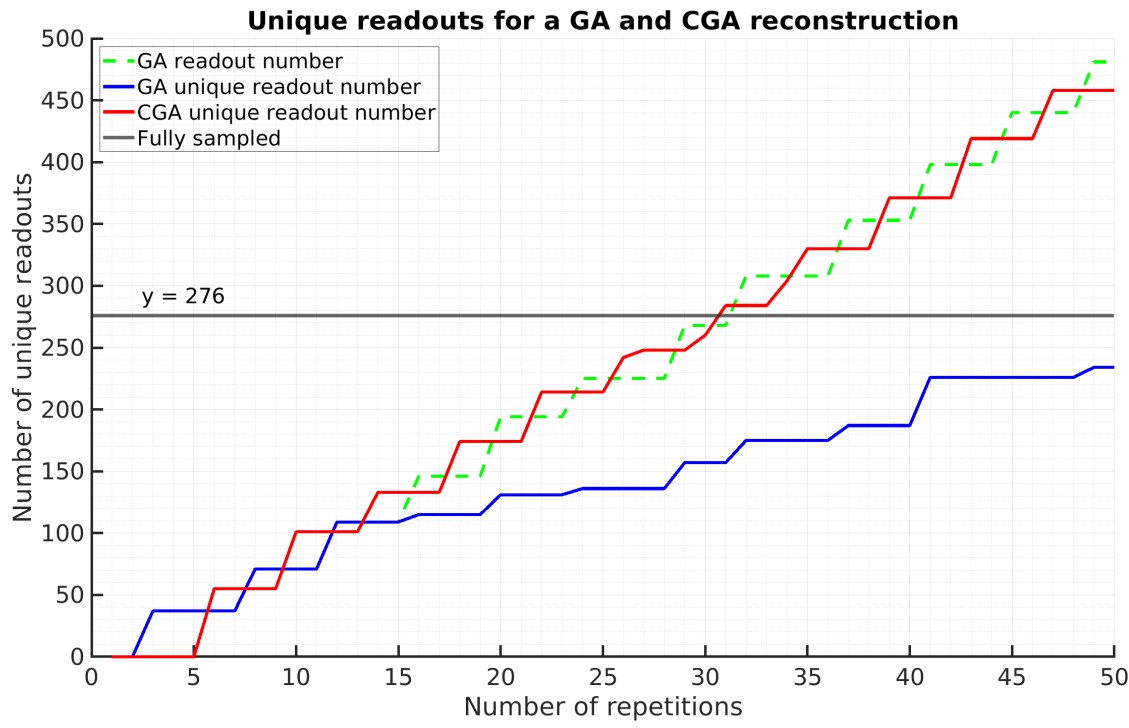


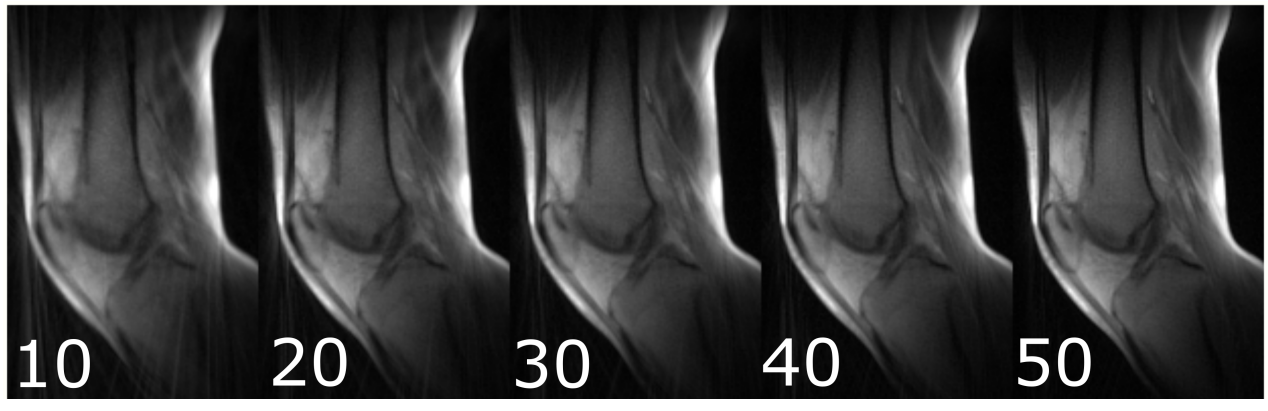
Fig. 37: Number of readouts for different number of repetitions for the GA and CGA measurements at the 25° angular position with angle window 2° . The number of readouts for GA and the number of unique readouts for CGA are approximately the same and appear to increase at the same rate. This is not the case for the number of unique readouts for GA, due to readouts having repeating radial positions.

Figure 36 shows the ROI centre of mass shift in the x (transverse) and z (longitudinal) direction from the 30 bpm, 60 bpm and 90 bpm sagittal measurements (during extension and flexion). The shifts range up to 1.3 voxels and 2 mm, which is comparable to the shifts from the transverse data. The standard deviation for the shifts in the sagittal plane shown in Table 4 suggest that the motion of the leg is similar in both x- and z-directions. The design of the device shown in Figure 17 does not include any specific measure to limit leg motion in the z-direction other than the ankle strap attached to the leg brace as shown in Figure 17. Both Figures 35 and 36 show that the leg is secured only to a limited extent in the x-, y- and z-directions during MR measurements. The transverse and sagittal shifts of the leg suggest that

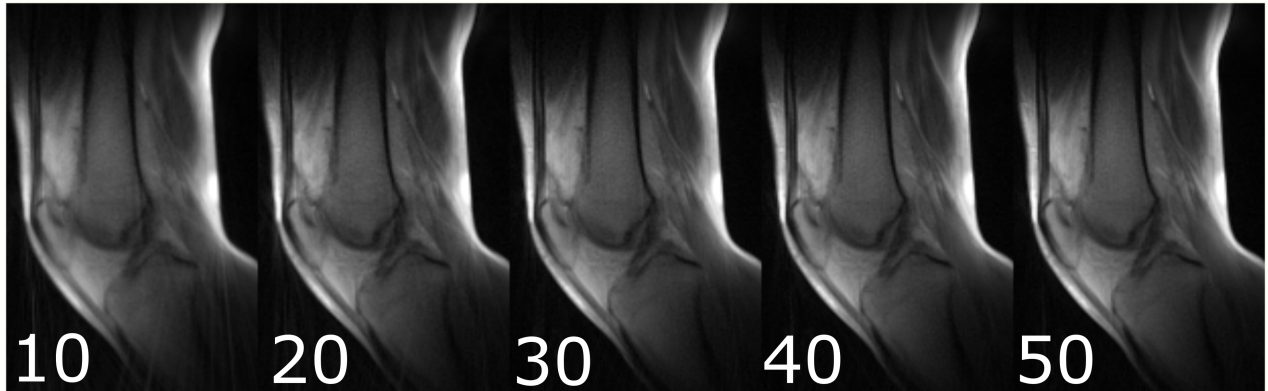
performing a longer measurement with many more flexion-extension cycles may not result in a more useful CINE reconstructed image for practical applications, due to blurring caused by the leg being in a different position in the device. Improving the design of the device will partly reduce the transverse and longitudinal leg motion. However, physiological motion of the subject will likely be a limiting factor in what is achievable.

E. Golden angle and continuous golden angle CINE images

Figure 37 shows the number of unique readouts for the golden angle (GA) and continuous golden angle (CGA) measurements for a 25° angular position and angle window 2° , based on the rotary encoder data. It can be seen that the number of unique readouts for the CGA measurement



(a)



(b)



(c)



(d)

Fig. 38: CINE images from the golden angle (a) and continuous golden angle (b) measurements at the 25° angular position with angle window 2° , reconstructed with readouts from 10, 20, 30, 40 and 50 repetitions. The number of unique readouts for different number of repetitions is shown in Figure 37.

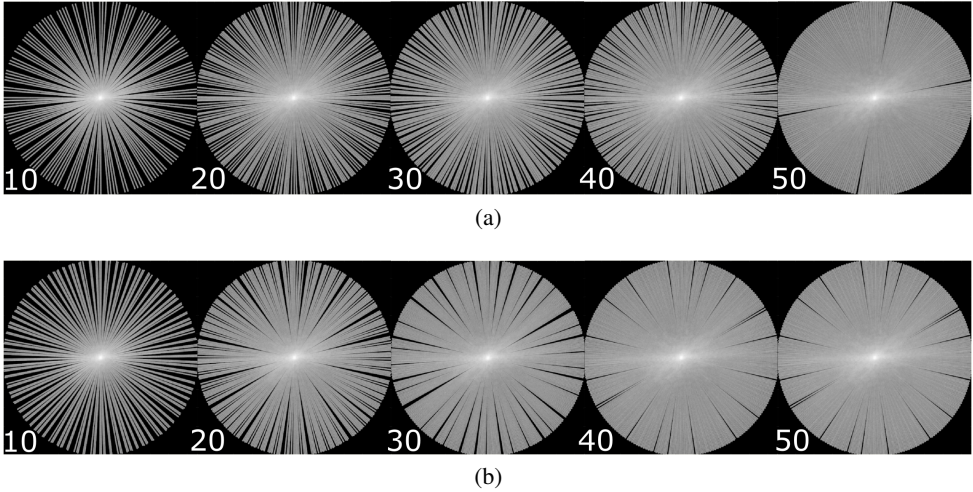


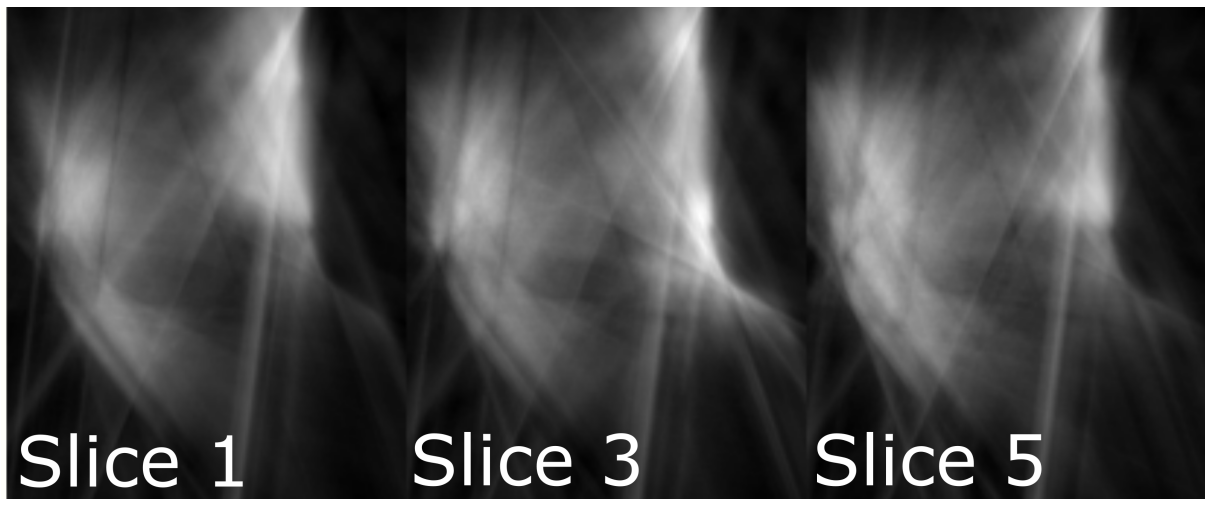
Fig. 39: Logarithmised magnitude of k-space of CINE images reconstructed for a different number of sequence repetitions from the golden angle (a) and continuous golden angle (b) measurements shown in Figure 38. The continuous golden angle sequence appears to fill the k-space shown faster than the golden angle sequence, with the exception of the 50 repetition reconstructions.

increase in a linear fashion, since each readout is unique. For the GA measurement, readouts have repeating positions and a fully sampled k-space requires more repetitions, as compared to the CGA case. This suggests that using the continuous golden angle method can reduce the number of repetitions necessary for a fully sampled k-space and consequently reduce measurement time. Figure 38 shows CINE reconstructed images for a different number of repetitions for both GA and CGA. From visual assessment, the CGA images appear to be sharper than the respective GA images, with a possible exception being the 50 repetition images. The k-space of the images, shown in Figure 39, support this comparison as CGA clearly samples a larger coverage of k-space than GA for 10-40 repetitions. In the 50 repetitions case from the figure, the k-space for GA appears to have fewer gaps than the k-space for CGA. However, as shown in Figure 37, the GA CINE reconstructed image at 50 repetitions does not have enough unique readouts for a fully sampled k-space compared to the CGA CINE reconstructed image. Overall,

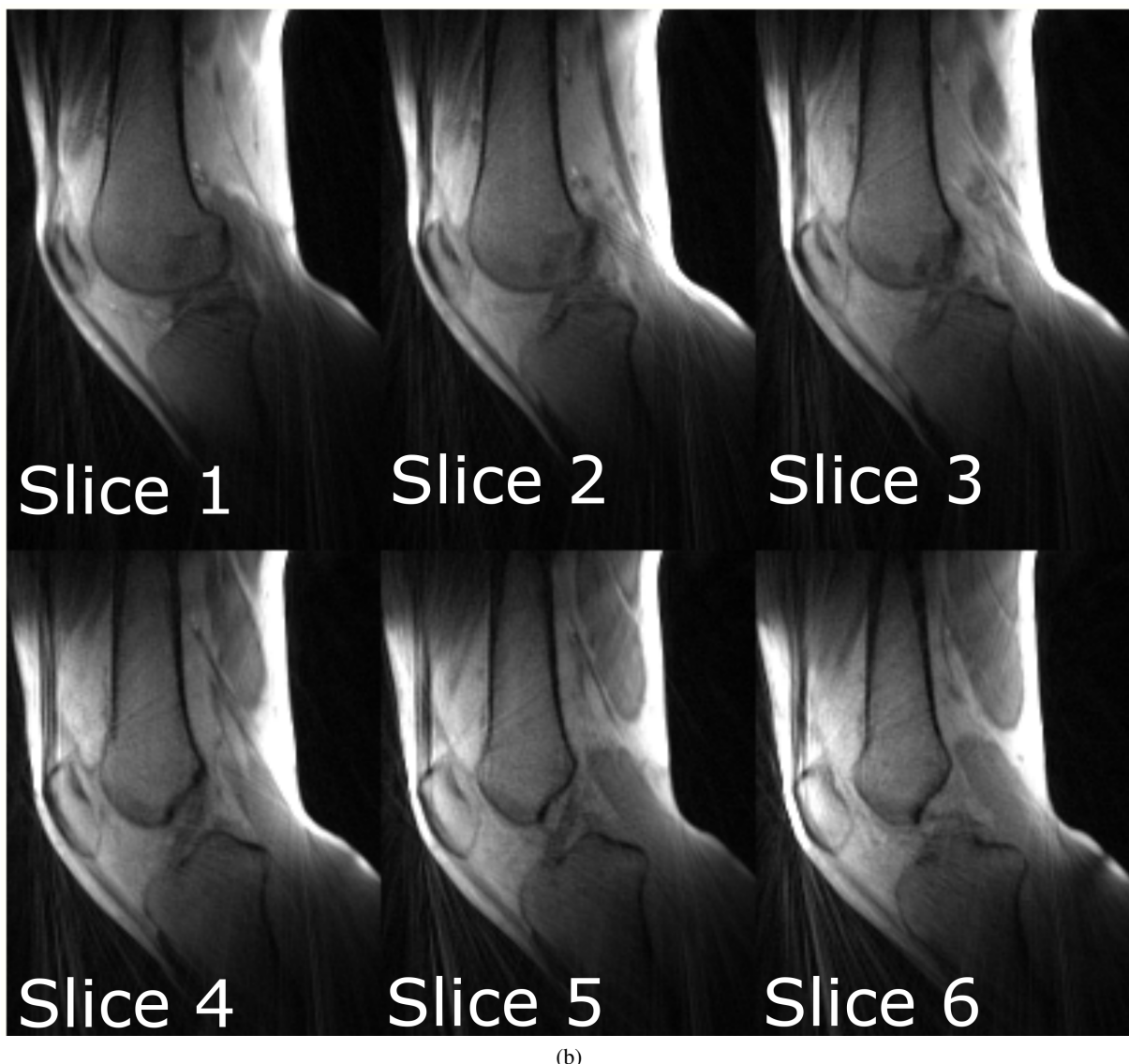
Figures 37, 38 and 39 suggest CGA to result in faster sampling of k-space compared to GA, due to there being no repeating radial readout positions. The CGA sequence therefore shows promise for conducting MR measurements with shorter measurement times, which is especially preferred in cases where the subject suffers from knee pain or discomfort.

F. Multi-slice and 3D UTE images

Figure 40 shows the real-time and CINE reconstructed images from the multi-slice (MS) measurement for the 25° angular position with angle window 2° . The real-time images appear to suffer substantially from streaking and undersampling artifacts, as compared to the CINE images. The streaking seen in the CINE reconstructed images in Figure 40 is particularly pronounced in the anatomical regions in close contact with the receive coils, namely above the patella tendon. The number of unique radial readouts for one slice of the CINE reconstruction can be seen in Table 5. To clarify, all slices have the same number of readouts.

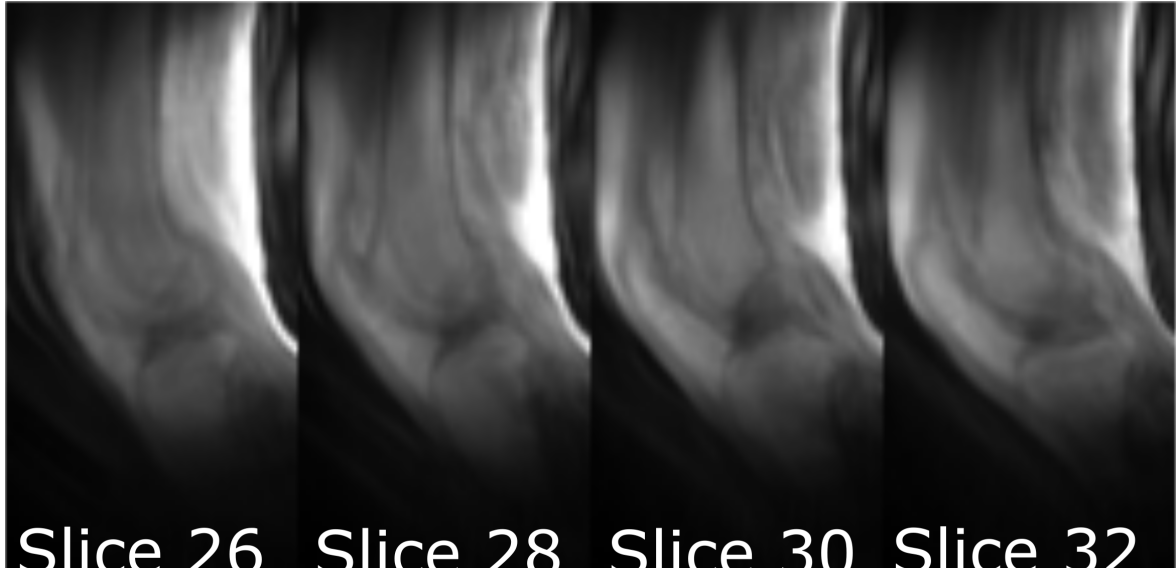


(a)

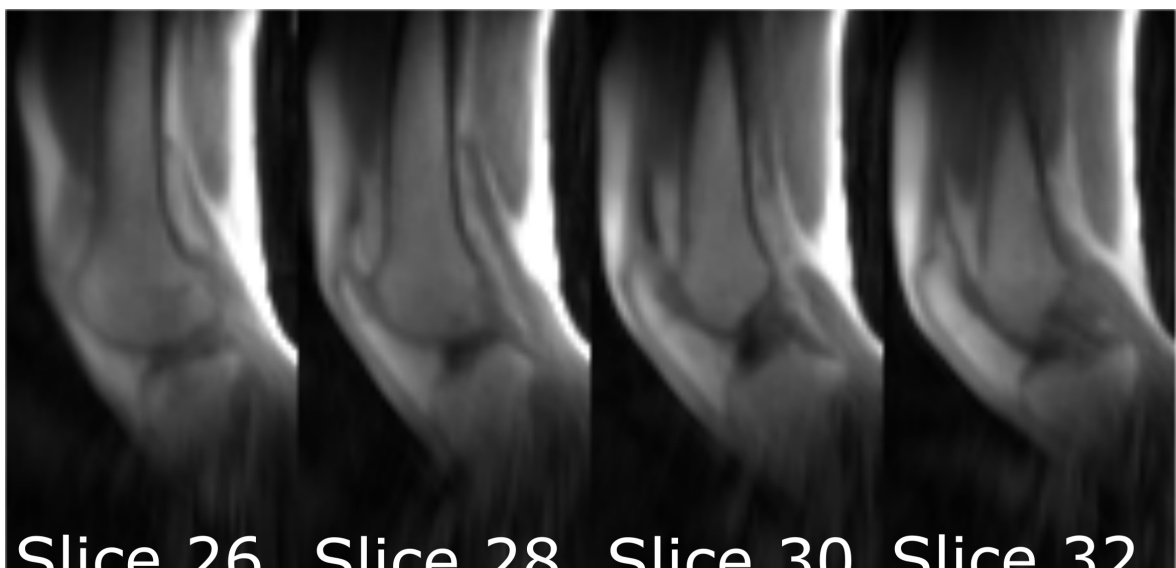


(b)

Fig. 40: Real-time (a) and CINE (b) reconstructed images from the multi-slice measurement for the 25° position with angle window 2° .



(a)



(b)

Fig. 41: Shown are 4 slices of a CINE reconstruction from the 3D UTE measurements without segmentation (a) and with segmentation factor 32 (b) for the 25° position with angle window 2° . The total number of slices recorded was 57.

Figure 41 shows the CINE images from the 3D UTE measurement without and with segmentation factor (SF) 32 for the 25° angular position with angle window 2° , respectively. The number of unique radial readouts of the two reconstructions along with the percentage of k-space sampling are shown in Table 5. It is worth noting that these numbers

represent the readouts for the entire 3D k-space (including all slices), not just the slices displayed in Figure 41. Visually comparing the reconstructed images from the two 3D UTE measurements, it can be seen that the images acquired with segmentation factor 32 appear sharper compared to those acquired without segmentation. The k-space

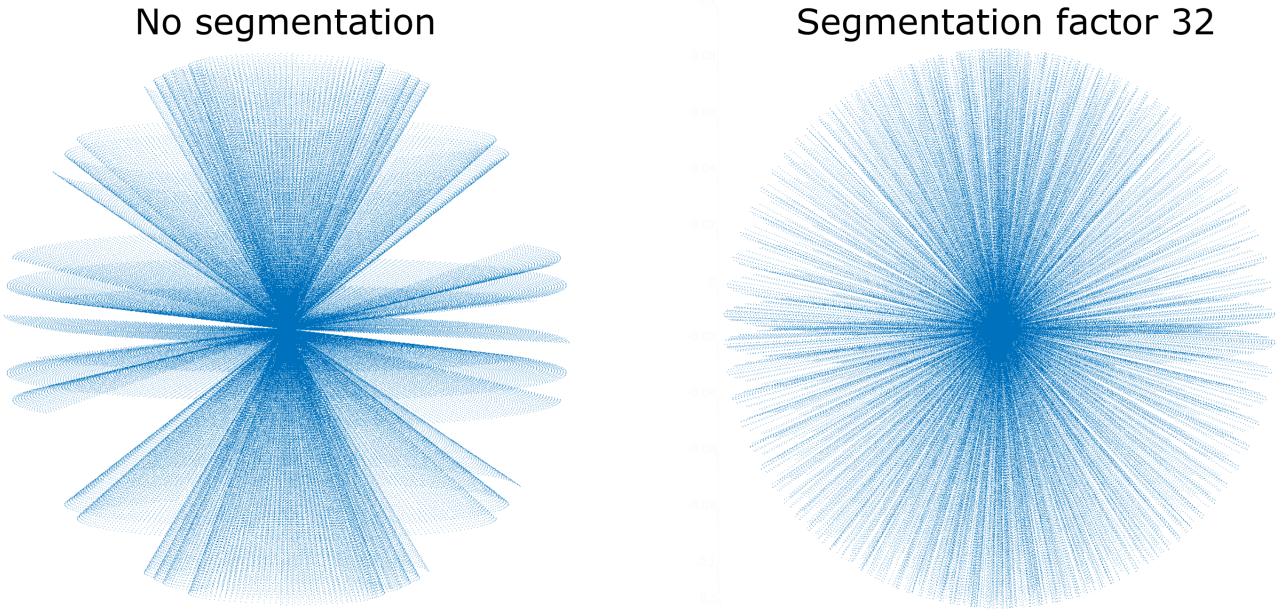


Fig. 42: Readouts distribution in k-space for the 3D UTE reconstructions without segmentation (left) and with segmentation factor 32 (right) shown in Figure 41. The 3D UTE measurement without segmentation results in gaps in k-space when reconstructing the CINE images from readouts selected by the angle window.

of the two reconstructions shown in Figure 42 can explain the reason for this difference. The k-space for the reconstruction from the 3D UTE measurement without segmentation appears to have significant gaps. The reason for this behaviour is not known, although one speculation is that the slow rate of readout acquisition and the rate of flexion-extension motion cycles are contributing factors. Nevertheless, by implementing a segmentation factor of 32, the order of readout acquisition is changed and results in a more evenly sampled k-space without any large gaps as shown in Figure 42.

Comparing the 3D UTE with segmentation data (Figure 41 (b)) with the MS data (Figure 40), it can be seen that the 3D UTE images have poorer spatial resolution than the MS images and have stronger blurring, likely resulting from undersampling in k-space. What 3D UTE offers is a spatial coverage of the entire knee with more slices, without gaps between slices and signal detection from

tissues with short T_2 values such as tendons and ligaments. The MS images look sharp, likely due to the continuous golden angle sequence, although some of them appear to suffer from streaking artifacts. The streaking artifacts could result from close contact between the receive coils and the skin, and from gaps in k-space because of the CGA sequence. Placing padding to increase the distance between the coils and the skin, and reconstructing images with more radial readouts (by increasing the angle window and/or increasing the number of sequence repetitions during measurement) will reduce the severity of the streaking artifacts in the CINE MS images. Both MS and 3D UTE result in a larger spatial coverage of the knee compared to a single 2D slice measurement and have different advantages depending on the intended application.

Reconstruction	MS	UTE	UTE SF32
Number of readouts	349	4765	5172
Number of unique readouts	349	2591	2811
Percentage sampled	126.5%	28.2%	30.6%

Table 5: Number of unique radial readouts and the percentage of sampled k-space for the single MS and two 3D UTE reconstructions (one without and two with segmentation factor 32 (SF32)). MS, UTE and UTE SF32 are shown in Figures 40 and 41 respectively. The percentage for the MS reconstruction are higher than 100%, because of the CGA sequence. It is worth noting that the percentage of sampled k-space has been defined here as the ratio of the number of unique radial readouts present in the reconstructed image (349 in the case of MS) to the number of unique readouts required for a fully sampled k-space (276 in the case of MS, calculated using equation 10).

G. Comparing CINE images of measurements with and without weight

Figure 43 shows a knee image from the 30 bpm measurement (using Protocol I) with weight overlaid with the absolute difference (shown in red) of itself and the image from the 30 bpm measurement without weight. Since the images were translated such that their tibia bone align, one expects the signal difference to indicate differences in tissues when the load on the knee is increased or decreased. For example, changing the load on the knee also changes the shape of the patellar tendon as shown in the red overlay of the figure. Another example of tissue shape changes is the area around the hamstrings (i.e., the posterior thigh muscles), possibly due to the leg pushing harder into the cushions or more blood flowing to the muscles, thereby increasing their volume. This demonstrates a potential application of using CINE reconstruction on dynamic MRI data to investigate the effect of load on knee tissue and joint mechanics, although further efforts are

required for analysis.



Fig. 43: CINE image from a 2D single slice measurement with weight, overlaid with the absolute difference of the image with a CINE image from a measurement without weight.

V. DISCUSSION

Regarding the rotary encoder data, subjects were generally able to perform flexion-extension motion cycles by following the metronome. On occasion, inconsistencies such as MC1 in Figure 30 or slightly different ranges of motion were observed which may require to discard the readouts at those particular regions of the motion curve. In the case of CINE, these inconsistencies do not prevent from image reconstruction, but rather would result in images with a higher or lower number of available readouts for individual leg positions. For example, if one were to reconstruct a CINE image at angular position 2° with angle window 2° based on the data shown in Figure 30, one would obtain a CINE image with fewer readouts, because not all motion cycles reach the angular position. Furthermore, it

would be desirable in this case that the motion cycles go down to 1° , as the angle window will include readouts between 3° and 1° . From the figure, it can be seen that the subject did not maintain a completely consistent leg motion, as there are regions where they moved their leg with slightly different speeds. Naturally, this is to be expected from human motion and it does not appear to have a significant effect of the CINE images.

Regarding the trigger pulses seen in Figure 30, there were inconsistencies in the distances from one rising flank to another rising flank with standard deviation $\sigma = 0.5 \text{ ms}$. This deviation likely results from the electrical conversion of the optical trigger pulses as the pulses are made longer because some input/output interfaces, such as the parallel, port are too slow for the original fast optical pulse. Since the time of acquiring radial readouts is approximated by the rising flanks of the triggers, their real time values might also be offset on average by 0.5 ms. In the context of image reconstruction, this does not have practical significance as the subject's leg would not have moved by a substantial amount during such a short time frame.

One effect of the angle window width on the real-time (RT) reconstructed images from Figure 32 is that a smaller window (such as the 1° used in this report) results in undersampling artifacts and poor spatial resolution. What specific angle window value will result in these undersampling artifacts will depend on the sequence, the motion speed of the subject and the number of repetitions. In general, however, there will be a limit to how small the angle window can be such that it results in practically useful images. Additionally, it is worth noting that a larger angle window will always reduce the APP (angular position precision)

and what APP is deemed to be acceptable will depend on the intended application. In the case of the RT images from Figure 32, it is unclear how to select what the best angle window width is, other than by visually assessing the images and the k-space sampling percentage. For example, RT AW3 and RT AW5 appear to be overall sharper than RT AW1 and RT AW2. RT AW5 has a fully sampled k-space as shown in Table 1 compared to RT AW3, although RT AW5 would have a worse APP than RT AW3 and will negatively impact morphological analysis due to blurring, especially near anatomical structures that change their position during measurements. This is why the CINE reconstructed images in the figure are better choices for practical application. They offer visibly comparable or better sharpness and better APP. CINE AW1 has better APP and CINE AW2 has a higher k-space sampling percentage. Therefore, there is a trade-off that must be considered that will likely depend on the desired application. Although it is difficult to determine the best angle window for a given reconstruction, it can be visually confirmed if a chosen angle window is too small or too large, typically due to the undersampling artifacts (such as in RT AW 1) or blurring (such as in RT AW 5 around the patella and patellar tendon) shown in Figure 32.

In the case of real-time reconstructions, measurements with a slower moving leg would result in more radial readouts acquired for a given angular position and angle window (assuming the same sequence parameters are used), thereby increasing the spatial resolution of the image without sacrificing temporal accuracy. However, slower motion is harder to do by the subjects and the motion at some point becomes unphysiological. For CINE reconstructions, measurements with more repetitions could improve the spatial resolution of an

image without lowering the speed of the leg motion. This would be preferable for research on joint and muscle mechanics where a faster moving leg may be desirable, as compared to a slower moving leg. However, even longer acquisitions might be challenging for patients/volunteers with previous injuries. The 30 bpm, 60 bpm and 90 bpm measurements were performed with a different number of repetitions to keep the number of motion cycled relatively the same. The different number of repetitions, however, changes the total number of readouts acquired during the measurements. To keep the total number of readouts the same across the three measurements, the CINE images shown in Figure 33 were all reconstructed with readouts from the first 80 repetitions. Table 2 suggests the CINE 90 bpm image to have a higher k-space sampling percentage than the CINE 60 bpm and CINE 30 bpm images. A reason for this could be the way readouts are distributed on the rotary encoder motion curve for a faster moving leg. To compare the three images with fully sampled k-space, performing these three measurements again with the same sequence parameters and a higher number of repetitions (where only the leg speed is changed), such that the k-space of a CINE image is fully sampled, might give more insight on how leg speed affects k-space sampling and spatial resolution. A possible drawback here could be if the subject finds it difficult to move their leg with a 90 bpm metronome tempo for 4 minutes, especially if they have a knee injury. Additionally, it is of interest for further study to perform MR measurements where the leg moves even faster, in order to find if there is a limit to how fast the leg can move such that CINE reconstruction is still feasible and what that limit is. This could prove to be a challenge, as metronome tempo of, for example 240 bpm (1 flexion-extension cycle every

2 seconds), could prove to be too difficult for the subjects to maintain and the measurement time will have to be reduced. At higher metronome tempos (such as 240 bpm or higher), appropriate subjects could be volunteering athletes or people leading a physically active lifestyle.

The images shown in Figure 31 were reconstructed with data where the leg was only moving in one direction, in this case during flexion. This was done due to the differences of images reconstructed from readouts acquired during both flexion and extension, in those areas with larger differences, as shown in Figure 22. It could be possible that either the concentric (in this case extension) or the eccentric (flexion) part of the motion is better suited for reconstruction. There are observations that eccentric motion requires less energy than concentric motion [31], which could give a reason for choosing one over the other. However, the weights used during measurements are likely not heavy enough for this to have a significant impact. Should the difference in signal be negligible, for example in already blurred images, readouts from both flexion and extension could be used to increase the number of unique readouts used for a CINE reconstruction and increase the k-space sampling percentage. However, analysis based on the images could be hindered by streaking and undersampling artifacts.

Increasing the number of repetitions of a measurement would result in CINE images being reconstructed from many motion cycles. As shown in Figures 35 and 36, the shifts of the bone region-of-interests suggest that the leg is not perfectly stable inside the device, which would cause blurring in CINE images. One reason for this instability could be the mechanics of the strap used to secure the subject's thigh, as it is not secured to the bottom of the device but rather to the attachment on the

elevated structure with the position sensor mount (shown in Figure 17). A method to improve this would be to create openings through the bottom of the device and fit the thigh strap through those openings. Other sources of instabilities could simply be the platform the leg rests on (in this case, the wooden blocks and cushions used for knee elevation), misalignment of the leg relative to the device and the free space available for sideways motion during measurements. A platform with a curved concave surface could help prevent sideways motion, by decreasing the available space on the sides of the thigh. Whether this idea would work in practice with the receiver coil placed at the bottom of the leg is a question for further study. Placing additional padding and cushions to the sides of the knee could also reduce potential sideways motion. Physiological sources of instability could be anatomical changes in the muscle such as viscoelasticity [32] or fluid accumulation, such as lactic acid [33], blood [34] and muscle water content [35], during the concentric and eccentric contractions. It is known that blood flow in the muscle is increased during dynamic exercise or rhythmic contractions [34]. These aforementioned changes could to some extent play a role during longer measurement sessions, faster leg motion and with larger resistance, as the intensity of the performed motion would increase. For the measurements performed in this work, these changes are believed to be negligible because of the relatively slow leg motion and small resistance.

Knowing that the device is not perfectly stable, the question then is whether there is a limit, and what that limit would be, to the number of useful repetitions for reconstructing a CINE image with a given angular position and angle window. Performing a longer measurement should give diminishing returns in terms of improving spatial resolution,

due to blurring resulting from instabilities. Finding a limit might provide a challenge as the images will be difficult to assess visually. One could say the limit would be when the k-space of an image is fully sampled and then visually, or using other methods, determine if adding more repetitions results in a better image.

The effects of shifts in leg position when comparing two CINE images, with and without weight, could be lessened by drawing regions-of-interest around the bones, translating them and aligning the images based on the translations. This method was used to obtain Figure 43. Images from high resolution data, such as the ones from Figure 34 could be a better choice for analysis as such artifacts do not seem to be present or strongly expressed, and drawing a region-of-interest could be achieved to a higher degree of accuracy. High resolution data could therefore be a preferable choice for any of the 2D single slice analysis done in this work, such as the region-of-interest centre of mass shifts from Figures 35 and 36 (where translating regions-of-interest was a challenge at times, due to real-time images being blurry) or the with and without weight application shown in Figure 43.

The golden angle and continuous golden angle data shown in Figure 37 suggest that CGA results samples k-space more than GA, with fewer sequence repetitions. This has a positive impact on CINE reconstructed images with fully sampled k-space, as both measurement time (by decreasing the number of repetitions) and APP (by decreasing the angle window) can be improved. It is then a question whether CGA is practically better than GA or if there is a drawback in using it. It has been shown that CGA can result in gaps in k-space even when there are enough radial readouts for a fully sampled k-space. This could be investigated

further by acquiring high resolution data with both GA and CGA, and comparing CINE reconstructed images for different angle windows, along with their k-space. If there are no significant drawbacks, CGA could be said to be an overall improvement from GA and could be used for further research on CINE reconstruction.

The multi-slice and 3D UTE measurements both give a larger spatial coverage of the knee compared to single slice measurements, from which CINE images can be reconstructed. 3D UTE with segmentation allows for better coverage of the knee with no gaps between slices, whereas MS with continuous golden angle results in significantly sharper images (despite the presence of streaking artifacts). Judging from the percentage of k-space sampling of the 3D UTE reconstructions from Table 5, further increasing the angle window would not seem to substantially improve the images or the k-space sampling and any improvement would come at the cost of a reduced APP. However, measurements with more repetitions and further reconstruction efforts, such as CG-SENSE [36] and Compressed Sensing [37], might give better results and more insight. The results from Table 5 suggest that there are repeating readout positions. As the UTE techniques used are 3D methods, implementing a continuous golden angle [38] technique could be non-trivial, especially due to the k-space being non-isotropic in the measurements performed in this work. Further efforts into using CGA along with 3D UTE with segmentation could improve the k-space sampling and the spatial resolution of CINE images. From the percentage of k-space sampling of the CINE images from the multi-slice measurement, it can be seen that the angle window could be decreased for better APP and the images would still have enough unique radial readouts for a 100% sampled k-space. However,

there would be an increase in streaking artifacts, resulting from the larger gaps in k-space due to the radial readout distribution of the CGA method. As all angles used in CGA are unique, gaps would naturally form when reconstructing an image at a given angular position and angle window. One method for reducing the gaps without further increasing the angle window, is to simply use more repetitions during the measurement, which would acquire more readouts, and fill the gaps.

In some measurements, the close contact with part of the receive coil resulted in significantly large signal from some channels. This can be noticed in nearly every image shown in this work, where a bright signal near the patella or the back of the thigh appear to be sources of streaking artifacts. One solution to the coils being in close contact with the leg is to add cushions to increase the distance.

VI. CONCLUSION

In this work, it has been demonstrated that CINE reconstruction from dynamic MRI data is possible with a device intentionally designed to allow repetitive and guided knee movement, and a rotary encoder. Visual comparison of images from CINE and real-time reconstruction methods showed that CINE images have overall better spatial resolution and will therefore be more useful for further research on joint and muscle mechanics of the knee. The reconstruction of CINE images from data with a different motion speed (16 s/cycle, 8 s/cycle and 5.3 s/cycle) has been shown to be possible without significant negative impact on spatial resolution, although further efforts are required to the upper limit of the motion speed, at which CINE reconstruction is still feasible with the current mechanical setup and sequences. In addition, CINE images have been demonstrated

for high resolution single slice, multi-slice and 3D UTE data. This makes CINE a versatile method, as multi-slice and 3D UTE images cannot be reconstructed for dynamic MRI data using real-time methods, due to the low number of readouts. The reconstructed MS and 3D UTE images shown suffer from streaking artifacts (for MS) and poor spatial resolution (for 3D UTE). However, these methods show potential in measuring a larger spatial coverage of the knee and further efforts could improve their performance.

Instability of the leg inside the device has been shown to result in shifts in the leg position in the x-, y- and z-directions, which contribute to blurring in the CINE images, as they are reconstructed with readouts from different motion cycles. One possibility for minimising the shifts could be to alter the device, in particular the location of the thigh strap, and changing the surface the knee rests on from a flat to a concave surface. Another solution is to use fewer repetitions when performing a measurement, which would reduce the number of flexion-extension motion cycles, yet also reduce the number of readouts available for reconstruction. To reconstruct images with fewer readouts, a continuous golden angle sequence could be used, as it has been shown to result in a fully sampled k-space for less repetitions compared to the golden angle sequence.

A potential application has been demonstrated where the absolute difference of two CINE images was calculated from MRI scans with a different load placed on the leg. By overlaying one of the two CINE images with the absolute difference, changes in tissue shape can be seen and further analysis on these changes could give insight into musculoskeletal mechanics of the knee. The versatility of CINE overall allows for such investigations of dynamic MRI data, making it a

useful technique which could be used to better our understanding of physiological and pathological joint and muscle mechanics.

REFERENCES

- [1] M. A. Bernstein, K. F. King, and X. J. Zhou., *Handbook of MRI Pulse Sequences*. Academic Press, 2003.
- [2] R. W. Brown, Y.-C. N. Cheng, E. M. Haacke, M. R. Thompson, and R. Venkatesan, *Magnetic Resonance Imaging*. John Wiley & Sons, Ltd, 2nd ed., 2014.
- [3] M. Callaghan, H. Guney, N. Reeves, D. Bailey, K. Doslikova, C. Maganaris, R. Hodgson, and D. Felson, “A knee brace alters patella position in patellofemoral osteoarthritis: a study using weight bearing magnetic resonance imaging,” *Osteoarthritis and Cartilage*, vol. 24, no. 12, pp. 2055–2060, 2016.
- [4] T. A. Gallagher, A. J. Nemeth, and L. Hacein-Bey, “An introduction to the fourier transform: Relationship to MRI,” *American Journal of Roentgenology*, vol. 190, no. 5, pp. 1396–1405, 2008. PMID: 18430861.
- [5] J. A. d’Arcy, D. J. Collins, I. J. Rowland, A. R. Padhani, and M. O. Leach, “Applications of sliding window reconstruction with cartesian sampling for dynamic contrast enhanced MRI,” *NMR in Biomedicine*, vol. 15, no. 2, pp. 174–183, 2002.
- [6] V. Rasche, R. W. D. Boer, D. Holz, and R. Proksa, “Continuous radial data acquisition for dynamic MRI,” *Magnetic Resonance in Medicine*, vol. 34, no. 5, pp. 754–761, 1995.
- [7] J. Budjan, P. Riffel, M. M. Ong, S. O. Schoenberg, U. I. Attenberger, and D. Hausmann, “Rapid cartesian versus radial acquisition: comparison of two sequences for hepatobilary phase MRI at 3 Tesla in patients with impaired breath-hold capabilities,” *BMC Medical Imaging*, vol. 17, p. 32, May 2017.
- [8] S. Winkelmann, T. Schaeffter, T. Koehler, H. Eggers, and O. Doessel, “An optimal radial profile order based on the golden ratio for time-resolved MRI,” *IEEE Transactions on Medical Imaging*, vol. 26, pp. 68–76, Jan 2007.
- [9] H. P. Wagemakers, P. A. Luijsterburg, E. M. Heintjes, M. Y. Berger, J. Verhaar, B. W. Koes, and S. M. Bierma-Zeinstra, “Outcome of knee injuries in general practice: 1-year follow-up,” *British Journal of General Practice*, vol. 60, no. 571, pp. e56–e63, 2010.
- [10] T. P. Andriacchi, A. Mündermann, R. L. Smith, E. J. Alexander, C. O. Dyrby, and S. Koo, “A framework for the in vivo pathomechanics of osteoarthritis at the knee,” *Annals of Biomedical Engineering*, vol. 32, pp. 447–457, Mar 2004.
- [11] A. Haase, “Snapshot FLASH MRI. applications to T1, T2, and chemical-shift imaging,” *Magnetic Resonance in Medicine*, vol. 13, no. 1, pp. 77–89, 1990.

- [12] M. Krämer, K.-H. Herrmann, J. Biermann, and J. R. Reichenbach, "Retrospective reconstruction of cardiac cine images from golden-ratio radial MRI using one-dimensional navigators," *Journal of Magnetic Resonance Imaging*, vol. 40, no. 2, pp. 413–422, 2014.
- [13] F. T. Sheehan, F. E. Zajac, and J. E. Drace, "Using cine phase contrast magnetic resonance imaging to non-invasively study *in vivo* knee dynamics," *Journal of Biomechanics*, vol. 31, no. 1, pp. 21–26, 1997.
- [14] U. H. Melchert, C. Schröder, J. Broßmann, and C. Muhle, "Motion-triggered cine MR imaging of active joint movement," *Magnetic Resonance Imaging*, vol. 10, no. 3, pp. 457–460, 1992.
- [15] I. Estermann, R. Frisch, and O. Stern, "Magnetic moment of the proton," *Nature*, vol. 132, pp. 169–170, Jul 1933.
- [16] F. Eggenschwiler, "B1-mapping and B1 inhomogeneity correction at high field," *Doctoral Dissertation at the ecole polytechnique federale de Lausanne*, 2015.
- [17] S. E. Barnes and S. Maekawa, "Generalization of Faraday's law to include nonconservative spin forces," *Phys. Rev. Lett.*, vol. 98, p. 246601, Jun 2007.
- [18] D. Torchia and A. Szabo, "Spin-lattice relaxation in solids," *Journal of Magnetic Resonance (1969)*, vol. 49, no. 1, pp. 107–121, 1982.
- [19] S. Currie, N. Hoggard, I. J. Craven, M. Hadjivassiliou, and I. D. Wilkinson, "Understanding MRI: basic MR physics for physicians," *Postgraduate Medical Journal*, vol. 89, no. 1050, pp. 209–223, 2013.
- [20] C. Westbrook and J. Talbot, *MRI in Practice*. Wiley Publishing, 5th ed., 2018.
- [21] Z. Wang, "Fast algorithms for the discrete w transform and for the discrete fourier transform," *IEEE Transactions on Acoustics, Speech, and Signal Processing*, vol. 32, no. 4, pp. 803–816, 1984.
- [22] M. Frigo and S. G. Johnson, "FFTW: An adaptive software architecture for the FFT," in *Proc. 1998 IEEE Intl. Conf. Acoustics Speech and Signal Processing*, vol. 3, pp. 1381–1384, IEEE, 1998.
- [23] H. Nyquist, "Certain topics in telegraph transmission theory," *Transactions of the American Institute of Electrical Engineers*, vol. 47, no. 2, pp. 617–644, 1928.
- [24] M. Livio, *The Golden Ratio: The Story of Phi, the World's Most Astonishing Number*. New York : Broadway Books, 2003.
- [25] M. H. Pui and E. C. Fok, "MR imaging of the brain: comparison of gradient-echo and spin-echo pulse sequences," *American Journal of Roentgenology*, vol. 165, no. 4, pp. 959–962, 1995. PMID: 7677001.
- [26] K.-H. Herrmann, M. Krämer, and J. R. Reichenbach, "Time efficient 3D radial ute sampling with fully automatic delay compensation on a clinical 3T MR scanner," *PLoS One*, vol. 11, pp. 1–16, 03 2016.
- [27] H. T. Fabich, M. Benning, A. J. Sederman, and D. J. Holland, "Ultrashort echo time (UTE) imaging using gradient pre-equalization and compressed sensing," *Journal of Magnetic Resonance*, vol. 245, pp. 116–124, 2014.
- [28] N. R. Zwart, K. O. Johnson, and J. G. Pipe, "Efficient sample density estimation by combining gridding and an optimized kernel," *Magnetic Resonance in Medicine*, vol. 67, no. 3, pp. 701–710, 2012.
- [29] T. Ono, T. Okuwaki, and T. Fukubayashi, "Differences in activation patterns of knee flexor muscles during concentric and eccentric exercises," *Research in Sports Medicine*, vol. 18, no. 3, pp. 188–198, 2010. PMID: 20623435.
- [30] S. J. Erickson, I. H. Cox, J. S. Hyde, G. F. Carrera, J. A. Strandt, and L. D. Estkowski, "Effect of tendon orientation on MR imaging signal intensity: a manifestation of the "magic angle" phenomenon," *Radiology*, vol. 181, no. 2, pp. 389–392, 1991. PMID: 1924777.
- [31] W. Herzog, "Why are muscles strong, and why do they require little energy in eccentric action?," *Journal of Sport and Health Science*, vol. 7, no. 3, pp. 255–264, 2018.
- [32] H. Oka, "Estimation of muscle fatigue by using EMG and muscle stiffness," in *Proceedings of 18th Annual International Conference of the IEEE Engineering in Medicine and Biology Society*, vol. 4, pp. 1449–1450 vol.4, 1996.
- [33] G. D. Lamb and D. G. Stephenson, "Point:Counterpoint: Lactic acid accumulation is an advantage/disadvantage during muscle activity," *Journal of Applied Physiology*, vol. 100, no. 4, pp. 1410–1412, 2006. PMID: 16540714.
- [34] M. H. Laughlin, "Skeletal muscle blood flow capacity: role of muscle pump in exercise hyperemia," *American Journal of Physiology-Heart and Circulatory Physiology*, vol. 253, no. 5, pp. H993–H1004, 1987. PMID: 3318504.
- [35] M. E. Sesto, R. G. Radwin, W. F. Block, and T. M. Best, "Anatomical and mechanical changes following repetitive eccentric exertions," *Clinical Biomechanics*, vol. 20, no. 1, pp. 41–49, 2005.
- [36] M. Usman, S. Latif, M. Asim, B.-D. Lee, and J. Qadir, "Retrospective motion correction in multishot MRI using generative adversarial network," *Scientific Reports*, vol. 10, p. 4786, Mar 2020.
- [37] B. Liu, Y. M. Zou, and L. Ying, "Sparsesense: Application of compressed sensing in parallel MRI," in *2008 International Conference on Information Technology and Applications in Biomedicine*, pp. 127–130, 2008.
- [38] R. W. Chan, E. A. Ramsay, C. H. Cunningham, and D. B. Plewes, "Temporal stability of adaptive 3D radial MRI using multidimensional golden means," *Magnetic Resonance in Medicine*, vol. 61, no. 2, pp. 354–363, 2009.

LIST OF FIGURES

1	Diagram of a spinning proton in the presence of an external field B_0 , with magnetic moment μ and precession frequency ω_0	6
2	The direction of M being rotated away from B_0 in a laboratory (a) and rotating (b) reference frame [16].	6
3	Recovery of the longitudinal magnetisation M_z following a 90° RF pulse. The recovery produces an exponential curve characterised by the T_1 time constant shown in equation (3) [19].	7
4	Transverse magnetisation M_{xy} decay following a 90° RF pulse. The decay produces an exponential curve characterised by the T_2 time constant shown in equation (4).	7
5	Slice selection centred at position z_0 along the z axis with thickness Δz , for an RF pulse with bandwidth $\Delta\omega$ and gradient G_z . Only the protons inside the blue-shaded region along the z axis will be excited.	8
6	Phase encoding along the y -direction	8
7	K-space representation of an image	8
8	Cartesian sampling of k-space	9
9	Radial sampling of k-space	9
10	Radial readouts based on a fixed increment and the golden angle	10
11	Sliding window reconstruction.	11
12	Gradient Echo sequence	11
13	Sketch of a 3D volume with 3 slices. The slices are separated by gaps shown in black.	11
14	3D distribution of readouts in k-space [26]. In (a), the coordinate system for the readouts is defined where each readout starts at the k-space centre and points to different end positions on a circle of constant latitude. Circles of different latitude form a spherical surface (b), resulting in a 3D distribution of readouts (c).	12
15	3D UTE sequence diagram for radial sampling of k-space. The diagram is shown for acquiring one readout. The readout gradient G_R is rotated in x , y and z to fill k-space according to the distribution shown in Figure 14.	12
16	Diagram (a) and high resolution image (b) of the knee with labeled anatomical structures.	13
17	Sketch (a) and photos (b) and (c) of the device with labeled components. The front part, with the weight platform, goes into the bore of the scanner first as shown in (c), and the rear part is where the subject lays and fits their leg through the leg brace, and where two MR receive coils are placed below and above the knee as shown in (b). Sandbags are placed under the subject's left leg for comfort.	14
18	The Graphical User Interface used to record data.	15
19	Rotary encoder data and trigger pulses sketch	16
20	Illustration of how the rotary encoder and radial readouts are synchronised.	17
21	Illustration of readout selection for RT and CINE reconstruction	18
22	Sagittal image showing differences in signal between flexion and extension	19

23	Sagittal CINE images reconstructed during flexion and extension	19
24	Receive coil channel signal reduction	19
25	Real-time reconstructed image from a transverse slice through the femur with a drawn region-of-interest drawn around the femur. Once the ROI is copied onto another real-time reconstructed frame and aligned with the femur bone, the ROI centre of mass will have a shift Δx and Δy in the x- and y-directions respectively.	22
26	Zoomed in image of the femur bone from the transverse scan of Figure 25 before (a) and after (b) using bicubic interpolation with factor 3.	22
27	Real-time reconstructed image from a sagittal slice through the knee with drawn region-of-interest around the tibia bone.	23
28	Golden Angle (GA) and Continuous Golden Angle (CGA) readout acquisition for 2 repetitions with 5 radial readouts each	24
29	K-space filling for 3D UTE with and without segmentation	25
30	Rotary encoder data for the 30 bpm measurement with weights	26
31	Real-time and CINE reconstructed images for 4 positions based on the rotary encoder data.	27
32	Real-time and CINE reconstructed images with different angle windows.	29
33	CINE reconstructed images from 3 data sets, with different motion speeds.	29
34	CINE reconstructed images from high resolution data set.	30
35	centre of mass shift for transverse data	32
36	centre of mass in the x and z-directions	33
37	Unique readouts for GA and CGA measurements	34
38	Golden angle and continuous golden angle images	35
39	Logarithmised magnitude of k-space of CINE images reconstructed for a different number of sequence repetitions from the golden angle (a) and continuous golden angle (b) measurements shown in Figure 38. The continuous golden angle sequence appears to fill the k-space shown faster than the golden angle sequence, with the exception of the 50 repetition reconstructions.	36
40	Real-time and CINE reconstructed images from the multi-slice measurement	37
41	CINE reconstructed images from the 3D UTE measurement without segmentation and with segmentation	38
42	Readouts distribution in k-space for the 3D UTE measurements.	39
43	With and without weight comparison	40

LIST OF TABLES

1	Number of calculated unique radial readouts and the percentage of sampled k-space for the real-time (RT) and CINE reconstructed images from a single slice 2D radial golden angle measurement shown in Figure 32.	28
2	Number of calculated unique radial readouts and the percentage of sampled k-space for CINE images from three sagittal measurements with different motion speeds shown in Figure 33.	30
3	Standard deviation σ of the region-of-interest centre of mass shift in x and y, shown in Figure 35, for real-time reconstructed images from five transverse measurements.	31
4	Standard deviation σ of the region-of-interest centre of mass shift in x and z, shown in Figure 36, for real-time reconstructed images from three sagittal measurements.	31
5	Number of unique radial readouts and the percentage of sampled k-space for the single MS and two 3D UTE reconstructions (one without and two with segmentation factor 32 (SF32)). MS, UTE and UTE SF32 are shown in Figures 40 and 41 respectively. The percentage for the MS reconstruction are higher than 100%, because of the CGA sequence. It is worth noting that the percentage of sampled k-space has been defined here as the ratio of the number of unique radial readouts present in the reconstructed image (349 in the case of MS) to the number of unique readouts required for a fully sampled k-space (276 in the case of MS, calculated using equation 10).	40

DECLARATION OF INDEPENDENT WORK

I, Martin Aleksandrov Aleksiev, do hereby declare that this work submitted to the Friedrich-Schiller-University for the degree M.Sc. Photonics was solely undertaken by myself and that no help was provided from other sources as those allowed. All sections of this work that use quotes or describe an argument or concept developed by another author have been referenced to show that this material has been adopted to support this thesis.

Place/Date

Signature
